# The intercomparison of selected cloud retrieval algorithms

T. Nauss[a,*], A.A. Kokhanovsky[b], T.Y. Nakajima[c],
C. Reudenbach[a], J. Bendix[a]

[a]Laboratory for Climatology and Remote Sensing, University of Marburg, Deutschhausstr. 10,
D-35032 Marburg, Germany
[b]Institute of Environmental Physics, Bremen University, Otto Hahn Allee 1, D-28334 Bremen, Germany
[c]JAXA/EORC, Harumi Island Triton Square, Office Tower X 22F, 1-8-10 Harumi, Chuo-ku,
Tokyo 104-6023, Japan

## Abstract

The paper is devoted to the comparison of selected cloud retrieval algorithms. In particular, the authors compare cloud optical thickness, liquid water path and effective droplet size as obtained from the algorithms developed at the Japan Aerospace Exploration Agency (JAXA) and US National Aeronautics and Space Administration (NASA) and a new simplified cloud retrieval algorithm that is based on the analytical solutions of the radiative transfer equations valid for optically thick weakly absorbing cloud layers. Over ocean all three retrievals show very close results but differences increase for a scene over land. This is mainly caused by uncertainties due to the unknown surface albedo, especially for the semi-analytical approach that is based on measurements at 0.86 μm, where the contribution from ground is particularly large. Still, the simplified analytical retrieval technique gives results comparable with much more advanced codes.
© 2005 Elsevier B.V. All rights reserved.

*Keywords:* Cloud properties; Radiative transfer; Inverse problems

\* Corresponding author.
*E-mail addresses:* nauss@lcrs.de (T. Nauss), alexk@iup.physic.uni-bremen.de (A.A. Kokhanovsky),
nakajima@eorc.jaxa.jp (T.Y. Nakajima).

## 1. Introduction

Clouds play an important role in the earth–atmosphere radiation budget and are recognized as a key modifier of climate (Platnick and Valero, 1995). Therefore many authors have developed techniques for cloud microphysical properties retrievals. In general, cloud properties are retrieved using some kind of look-up table (LUT) approach (Liou and Wittman, 1979; Arking and Childs, 1985; Nakajima and King, 1990; Han et al., 1994; Nakajima and Nakajima, 1995) where pre-calculated radiative transfer results are iteratively lined with actual measured values in the visible and near-infrared regions of the electromagnetic spectrum. For cirrus clouds some authors also developed algorithms solely dependent on infrared channels (Ackerman et al., 1990; Strabala et al., 1994). Baum et al. (1994, 2003) as well as Pérez et al. (2000) proposed a night-time retrieval for all cloud types. The developed retrievals are in general validated against theoretically derived datasets or in-situ flight measurements. While the former type of validation shows the range of errors due to the concept or numerical uncertainties of the algorithms, the latter in general only allows to make rough assumptions of the retrieval accuracy mainly because of inhomogeneity of cloud fields, different measurement heights (e.g., satellite measurements, in-situ data at mid-level of a cloud, etc.) and sample volumes. Since many different retrievals are used in national and international research projects, it is of great importance to study the expected deviations between them. This will facilitate their use in climate research and also contribute to the solutions of many other atmospheric problems.

Therefore, three commonly used microphysical cloud property retrievals will be compared in this study. These are the LUT-based approach ATSK3 developed by Nakajima and Nakajima (1995) with the modification of Kawamoto et al. (2001), the LUT-based MOD06 approach by Platnick et al. (2003) and the semi-analytical cloud retrieval algorithm SACURA of Kokhanovsky et al. (2003). The retrievals are compared using data from the MODIS sensor on-board of the NASA EOS Terra satellite (King and Greenstone, 1999a) over both land and ocean. Note that these three techniques have been developed for different instruments, namely for the MoDerate resolutIon Spectroradiometer (MODIS, NASA) (King et al., 1992), the GlobaL Imager (GLI, JAXA) (Nakajima et al., 1998), and the SCanning IMaging Absorption spectroMeter for Atmospheric ChartographY (SCIAMACHY, European Space Agency) (Bovensmann et al., 1999). Algorithms are capable to retrieve also many other cloud parameters including cloud-top height. However, we compare only retrieval results for the effective radius, liquid water path, and cloud optical thickness and only the case of liquid clouds is considered. The retrievals for ice clouds are generally less accurate due to the complexity of light transport through highly inhomogeneous crystalline clouds (Min et al., 2004).

The results from all three algorithms are freely available at the internet (MOD06: http://www.daac.gsfc.nasa.gov/, ATKS3: http://isswww.eoc.jaxa.jp/iss/en/index.html, and SACURA: http://www.iup.physik.uni-bremende/scia-arc). Selected cloud algorithms as applied to MODIS and Meteosat-8 data can be found at http://www.lcrs.de.

Section 2 gives a brief overview of the three retrieval techniques and Section 3 shows the results of the comparison for two scenes over ocean and land. Section 4 is devoted to studies of the sensitivity of retrievals to auxiliary data.

## 2. Cloud retrieval algorithms

### 2.1. Basic concepts of cloud retrieval algorithms

All commonly used daytime cloud microphysics retrievals rely on the well-known characteristics of the reflection function at a non-absorbing (mainly visible) and an absorbing (near-infrared) wavelength. Fig. 1 shows the fundamental principle behind retrievals for wavelengths of 0.65 μm and 1.6 μm in which continuous lines represent equal effective radii while dashed lines stand for equal values of the optical thickness. It is evident that the reflection function at the non-absorbing wavelength is mainly a function of the cloud optical thickness $\tau$ and the absorbing wavelength signal is largely determined by the effective radius $a_{ef}$. Clearly, the reflection function saturates as $\tau \rightarrow \infty$. Hence, no information on $\tau$ can be retrieved for optically very thick clouds. It should be stressed that the saturation level is reached for lower $\tau$ for increasing absorbing wavelengths. Note that similar saturation appears with increasing cloud effective radius $a_{ef}$ for absorbing wavelengths.

Besides this, all operational retrieval algorithms are based on the 1-D radiation concept where a cloud is regarded as a plane-parallel, vertically and horizontally homogeneous layer which completely covers a remotely sensed picture element. Since real world clouds do not satisfy this concept (Loeb and Davies, 1996) and the cloud retrieval techniques are heavily based on the assumption of a plane-parallel homogeneous layer, the resulting microphysical parameters obtained from satellite cloud observations can only be interpreted as values which a homogeneous cloud would have if it has the same radiative characteristics as the observed ones. Horizontal and vertical inhomogeneities can induce an additional photon transport not accounted by 1-D models and structured cloud tops can further increase local cloud brightening or shading and therefore further increase the gap between retrieved and in-situ microphysical properties (see, e.g., Várnai, 2000; Nikolaeva
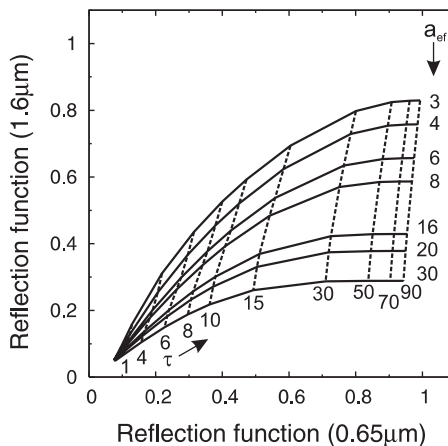


Fig. 1. Reflection of a water cloud at 0.65 μm and 1.6 μm with sun zenith 0° and nadir observation as a function of optical thickness (dashed lines) and effective cloud droplet radius (solid lines).

et al., 2005). These 3-D radiation effects can be accounted for by 3-D cloud models but actual computer speed is not sufficient for an operational application. Beside these 3-D effects, the presence of broken clouds leads to the underestimation of the optical thickness and overestimation of the effective cloud droplet radii by satellite measurements for ground surfaces darker than a cloud under study. For brighter surfaces, the opposite is true. Uncertainties in atmospheric water vapour content can result in significant deviations especially when using 2.1-μm or 3.7-μm wavelengths. Comparisons with in-situ aircraft measurements are also biased by different dimensions and possibly different altitudes of sampling volumes as well as general uncertainties in geolocation. Deviations of up to 15–30% are commonly found (Nakajima et al., 1991; Kawamoto et al., 2001). For an overview of such error sources see Han et al. (1994, 1995).

On this background, at least two conclusions can be drawn. The first is that sensitivity studies based on 1-D cloud model simulations are of great importance for the investigation of numerical uncertainties in the retrieval algorithms itself. Secondly, all algorithms retrieve only one possible realization of real world situations. Since resulting cloud parameters are commonly used in many climate research projects from case studies to operational general circulation models (Twomey, 1991; Austin et al., 1995; Kiehl, 1994), it is indispensable to compare the results of such retrievals against each other to get an idea of uncertainties solely traced back to the application of two different algorithms. Therefore an intercomparison of three cloud property retrievals is presented in this study. These are the retrieval part of the MODIS MOD06 product (King et al., 1997; Platnick et al., 2003), the LUT approach of Nakajima and Nakajima (1995) (see also Kawamoto et al., 2001) and the semi-analytic approach of Kokhanovsky et al. (2003).

## 2.2. JAXA look-up table approach ATSK3

The JAXA LUT approach is based on the technique of Nakajima and Nakajima (1995) with the modification of Kawamoto et al. (2001) using measurements at 0.65 μm, 3.7 μm and 11 μm. On the basis of a three-layer atmospheric model, the cloud signal is decoupled from the measured reflection functions and corresponding microphysical parameters collectively closest to the spectral cloud signal are extracted using several LUTs. The lowest atmospheric layer extends from the ground surface to the cloud bottom (index b), the middle layer encompasses the cloud layer (index c) and the upper layer ranges from the cloud top to the satellite (index a). The sensor signal in the visible range (without absorption) can be divided into the cloud signal and the contribution from beneath the cloud according to the following equation (Kawamoto et al., 2001):

$$L_{obs}(\tau, a_{ef}) = L_c(\tau_c, a_{ef}) + \Theta(\tau, a_{ef}) \frac{A_g}{1 - \bar{r}_c(\tau_c, a_{ef})A_g} \Theta(\tau, a_{ef}) \frac{\mu_0 F_0}{\pi}. \tag{1}$$

$L_{obs}$ is the observed radiance, $\mu_0$ the cosine of the solar angle, $F_0$ the extraterrestrial solar flux, $L_c$ the solar radiance reflected by the cloud layer, $\bar{r}_c$ the spherical albedo of the cloud, $\Theta$ the unidirectional flux transmissivity and $A_g$ is the ground albedo.

In the near-infrared range, absorption processes have to be taken into account and

$$
\begin{aligned}
L_{\mathrm{obs}}(\tau, a_{\mathrm{ef}}) = {} & \Theta_{\mathrm{a}} L_{\mathrm{c}}(\tau_{\mathrm{c}}, a_{\mathrm{ef}})\Theta_{\mathrm{a}} + \Theta_{\mathrm{a}}[1 - \Theta_{\mathrm{c}}(\tau_{\mathrm{c}}, a_{\mathrm{ef}}) - r_{\mathrm{c}}(\tau_{\mathrm{c}}, a_{\mathrm{ef}})]B(T_{\mathrm{c}}) \\
& + \Theta_{\mathrm{a}}\Theta_{\mathrm{c}}(\tau_{\mathrm{c}}, a_{\mathrm{ef}})\Theta_{\mathrm{b}} \frac{1 - A_{\mathrm{g}}}{1 - \bar{r}_{\mathrm{c}}(\tau_{\mathrm{c}}, a_{\mathrm{ef}})A_{\mathrm{g}}} B(T_{\mathrm{g}}) \\
& + \Theta_{\mathrm{a}}\Theta_{\mathrm{c}}(\tau_{\mathrm{c}}, a_{\mathrm{ef}})\Theta_{\mathrm{b}} \frac{A_{\mathrm{g}}}{1 - \bar{r}_{\mathrm{c}}(\tau_{\mathrm{c}}, a_{\mathrm{ef}})A_{\mathrm{g}}} \Theta_{\mathrm{b}}\Theta_{\mathrm{c}}(\tau_{\mathrm{c}}, a_{\mathrm{ef}})\Theta_{\mathrm{a}} \frac{\mu_0 F_0}{\pi} \\
& + f_{\mathrm{a}}(w_{\mathrm{ea}}, B(T_{\mathrm{c}}), \mu) + \Theta_{\mathrm{a}}(w_{\mathrm{eq}})\Theta_{\mathrm{c}}(\tau_{\mathrm{c}}, a_{\mathrm{ef}})f_{\mathrm{b}}(w_{\mathrm{ea}}, B(T_{\mathrm{g}})),
\end{aligned}
\tag{2}
$$

is composed of the transmission corrected cloud signal for a black underlying surface (first term), the emission from the cloud layer (second term) and both emission and reflection from the underlying surface (third and fourth terms, respectively). Moreover, atmospheric emission above and below the cloud layer is accounted by the last two terms and reflection of emitted radiation is neglected. $B$ is the Planck function of the cloud-top and ground temperature $T_{\mathrm{c}}$ and $T_{\mathrm{g}}$, $r_{\mathrm{c}}$ the unidirectional flux reflectivity of a cloud and $f$ the atmospheric thermal emission. The dependence of variables in Eq. (2) on the solar and observation angles and also on the cloud geometrical thickness is suppressed.

Kawamoto et al. (2001) showed that using the equivalent water vapour amount $w_{\mathrm{e}}$ for the calculation of atmospheric transmission, the results are nearly independent of the vertical water vapour profile. Therefore, this parameter is used for the LUT-based atmospheric absorption correction of the measured signal instead of a prescribed water vapour profile only valid for quite limited numbers of atmospheric stratifications. Note that $w_{\mathrm{e}}$ is defined as

$$
w_{\mathrm{e}} = \int w(z)\left[\frac{P(z)}{P_{\mathrm{g}}}\right]^{0.9}\left[\frac{T_{\mathrm{g}}}{T(z)}\right]^{0.5} \mathrm{d}z,
\tag{3}
$$

with the vertical profile of water vapour $w(z)$, air pressure $P(z)$ and air temperature $T(z)$ and corresponding ground values $P_{\mathrm{g}}$ and $T_{\mathrm{g}}$ (note that symbols used in equations are given also in Appendix A).

The microphysical parameters are retrieved by separating the cloud signal from the measured radiances and iteratively lining the extracted cloud signals with the pre-calculated values. The LUTs necessary for both processes (see Nakajima and Nakajima, 1995; Kawamoto et al., 2001) have been calculated with respect to MODIS channel 1 (0.65 μm), 20 (3.7 μm) and 31 (11 μm) characteristics using the RSTAR-5b radiative transfer model (Nakajima and Tanaka, 1986, 1988) for each combination of the input parameters shown in Table 1. Besides the LUTs, several auxiliary datasets are necessary for the retrieval. The vertical profiles for the calculation of $w_{\mathrm{e}}$ are taken from actual radiosonde data and $T_{\mathrm{g}}$ of cloudy pixels is computed by a multiple linear regression taking into account the ground temperature of surrounding cloud-free pixels, latitude and longitude coordinates and height above sea level. For surface albedo, a 14-day floating mean composite of cloud-free scenes is used similar to Lucht et al. (2000). Necessary atmospheric correction is performed using the 6s (Second Simulation of the Satellite Signal in the Solar Spectrum) radiative transfer code (Vermote and Roger, 1996; Vermote et al., 1997a,b).

Table 1
Grid system used for the calculation of the LUT tables for the ATSK3 retrieval

| $\tau$ | 1, 2, 4, 6, 9, 14, 20, 30, 50, 70 |
| --- | --- |
| $a_{\mathrm{ef}}$ (μm) | 2, 4, 6, 9, 12, 15, 20, 25, 30, 35, 40 |
| $T_c$ (K) | 250, 260, 270, 280, 290, 300 |
| $\vartheta_0$ (deg.) | 0, 5, 10, 20, 30, 35, 40, 45, 50, 55, 60, 65, 70 |
| $\vartheta$ (deg.) | 0, 5, 10, 20, 30, 35, 40, 45, 50, 55, 60, 65, 70 |
| $\phi$ (deg.) | 0, 10, 20, 30, 40, 50, 60, 70, 80, 90, 100, 110, 120,. . ., 180 |

The validation of the inversion technique described above has been performed by Kawamoto et al. (2001). Compared to theoretically calculated radiances, the validation shows only small deviations of never more than 6% which is equivalent to an absolute change of $\pm 1$ for the resulting optical thickness and $\pm 1$ μm for the effective radius. A comparison with in-situ aircraft measurements shows also a good agreement with in general less than 15% deviation.

## 2.3. Semi-analytical approach SACURA

In contrast to the commonly used LUT approaches, Kokhanovsky et al. (2003) developed a semi-analytical cloud retrieval using the asymptotic solutions (Germogenova, 1963; King, 1987) of the radiative transfer theory. According to van de Hulst (1980) the reflection function in a non-absorbing (subscript 0) spectral band can be written as

$$R_0(\mu, \mu_0 \phi, \tau) = R_\infty^0 (\mu, \mu_0, \phi) - t_0(\tau) K_0(\mu) K_0(\mu_0). \tag{4}$$

with the cosine of the solar and observation angle $\mu_0$ and $\mu$ and the relative azimuth angle $\phi$.

The diffuse transmittance $t_0$ is given by

$$t_0 = \frac{1}{0.75\tau(1 - g_0) + \alpha}, \tag{5}$$

with the asymmetry parameter $g$ and parameter $\alpha \approx 1.07$ defined in Eq. (12). The escape function $K_0(\mu)$ can be approximated with an accuracy of 2% (Kokhanovsky, 2004b) at $\mu > 0.2$ by

$$K_0(\mu) = \frac{3}{7}(1 + 2\mu). \tag{6}$$

Eqs. (4)–(6) reduce the calculation of the reflection function of a finite cloud to that of a semi-infinite one, where $R_\infty^0(\mu, \mu_0, \phi)$ only depends on the phase function and even this dependence is rather weak (Kokhanovsky, 2004a). $R_\infty^0(\mu, \mu_0, \phi)$ itself can be parameterized (Kokhanovsky, 2004b,c) but errors increase with increasing satellite zenith angles and exceed 5% for satellite zeniths larger $30°$ and solar zenith angles larger $60°$ (Kokhanovsky, 2004c). For nadir measurements the error is below 5% for all solar zenith angles except very low sun positions close to the horizon. Such low solar angles are not suitable for cloud retrievals.

While for single case studies with suitable observation geometries the SACURA retrieval performs well with this approximation (Kokhanovsky et al., 2005), it is not

suitable for operational full-disc applications using geostationary sensors. Therefore $R_\infty^0(\mu,\mu_0,\phi)$ is calculated for a $1°$ grid using the exact radiative transfer code of Mishchenko et al. (1999) for a modified gamma distribution and effective radius of 6 μm whereby the influence of $a_{\rm ef}$ on $R_\infty^0(\mu,\mu_0,\phi)$ is negligible (Kokhanovsky, 2004c). Along with a standard 3-D interpolation algorithm these pre-calculated values are used to compute $R_\infty^0(\mu,\mu_0,\phi)$ for the actual viewing geometry.

In the near-infrared range the reflection function of an absorbing cloud is given by

$$R(\mu,\mu_0\phi,\tau) = R_\infty(\mu,\mu_0,\phi) - \frac{mle^{-2\gamma\tau}}{1 - l^2 e^{-2\gamma\tau}} K(\mu)K(\mu_0), \tag{7}$$

with the reflection function of a semi-infinite absorbing cloud $R_\infty(\mu,\mu_0,\phi)$ and escape functions of absorbing media $K$. The parameters $m$, $l$, $\gamma$, and the escape function can be found from the solution of integral equations (Nakajima and King, 1992). This equation is used in the NASA MOD06 algorithm for large values of $\tau$. SACURA uses the following exponential solutions (Zege et al., 1991; Kokhanovsky et al., 2003),

$$R_\infty(\mu,\mu_0,\phi) = R_\infty^0 e^{-yu(\mu,\mu_0,\phi)}, \tag{8}$$

$$mK(\mu)K(\mu_0) = (1 - e^{-2y})K_0(\mu)K_0(\mu_0), \tag{9}$$

$$l = e^{-\alpha y}, \tag{10}$$

which are valid if the probability of photon absorption is small. This is usually the case for water clouds in visible and near-infrared (Kokhanovsky, 2004a). Taking into account that

$$y = 4\sqrt{\frac{1-\omega}{3(1-g)}}, \tag{11}$$

$$\alpha = 3\int_0^1 K_0(\mu)\mu^2 {\rm d}\mu = 1.07, \tag{12}$$

$$u(\mu,\mu_0,\phi) = \frac{K_0(\mu)K_0(\mu_0)}{R_\infty^0(\mu,\mu_0,\phi)}, \tag{13}$$

with the single scattering albedo $\omega$, Eq. (7) can be written as

$$R(\mu,\mu_0,\phi) = R_\infty(\mu,\mu_0,\phi) - te^{-x-y}K_0(\mu)K_0(\mu_0), \tag{14}$$

with the global transmittance

$$t = \frac{\sinh y}{\sinh(\alpha y + x)}, \tag{15}$$

and

$$\gamma = \sqrt{3(1-\omega)(1-g)}, \tag{16}$$

$$x = \gamma\tau. \tag{17}$$

Additional consideration of ground reflectance $A_g$ as in Eq. (1) yields to the two basic equations of SACURA for the visible

$$\hat{R}_0(\mu, \mu_0, \phi, \tau) = R_0(\mu, \mu_0, \phi, \tau) + \frac{A_g t_0^2 K_0(\mu) K_0(\mu_0)}{1 - A_g \bar{r}_c}, \qquad (18)$$

and near-infrared

$$\hat{R}(\mu, \mu_0 \phi) = R_\infty(\mu, \mu_0, \phi) - \left( e^{-x-y} - \frac{A_g t}{1 - A_g \bar{r}_c} \right) t K_0(\mu) K_0(\mu_0), \qquad (19)$$

spectral range. The relationships between parameters $(x,y)$ and values of the effective radius $a_{ef}$ and liquid water path LWP can be obtained from Mie theory but for SACURA we use parameterizations as described by Kokhanovsky et al. (2003). It is important that no new functions (as compared to the non-absorbing case) appear in Eq. (19).

It follows from Eq. (5) that

$$\tau_0 = \frac{4 \left( t_0^{-1} - \alpha \right)}{3 \left( 1 - g_0(a_{ef}) \right)}, \qquad (20)$$

but since $g_0$ is dependent on $a_{ef}$, $\tau_0$ cannot be calculated accurately using spectral measurements from the visible range alone. Moreover the transmission in the near-infrared region is dependent not only on $a_{ef}$ but also on LWP. Note that it follows approximately (Kokhanovsky, 2004b): $g_0 = 0.88 - 0.5(2\pi a_{ef}/\lambda)^{(-2/3)}$. Alternatively, the optical thickness can be expressed by the following approximate formula (Kokhanovsky, 2004b)

$$\tau_0 = \frac{3 LWP}{2 \rho a_{ef}} \left( 1 + \frac{1.1}{(2\pi a_{ef}/\lambda_1)^{2/3}} \right) = LWP \, \bar{k}_{ext}, \qquad (21)$$

with the density of water $\rho$. By combining with Eq. (20) we get

$$LWP = \frac{4 \left( t_0^{-1} - \alpha \right)}{3 \bar{k}_{ext} (\lambda_1, a_{ef}) (1 - g_0(a_{ef}))}, \qquad (22)$$

with

$$t_0 = \left[ \frac{K_0(\vartheta) K_0(\vartheta_0)}{R_\infty^0 - \hat{R}_0} - \frac{A_{g_0}}{1 - A_{g_0}} \right]^{-1}, \qquad (23)$$

from Eq. (18). The value of $\overline{k_{ext}}$ is related to the size of droplets by Eq. (21) (see, e.g., Kokhanovsky et al., 2003). Using Eq. (22) the dependence of $\tau$ on LWP in Eq. (19) can be accounted for by substituting Eq. (22) with $t_0$ from Eq. (23) in Eq. (19). This yields a single transcedent equation for the retrieval of $a_{ef}$ which can be easily solved numerically. Knowing $a_{ef}$, the optical thickness can be calculated using Eq. (20). The necessary substitution of $\tau$ by $\tau_0$ is done using a conversion function dependent on $a_{ef}$ (Kokhanovsky et al., 2004).

Kokhanovsky and Rozanov (2003) proposed a modification of the exponential approximations by substituting

$$t \rightarrow t - t_\Delta, \tag{24}$$

$$u(\mu, \mu_0, \phi) \rightarrow (1 - 0.05y)u, \tag{25}$$

with

$$t_\Delta = \frac{4.86 - 13.08\mu\mu_0 + 12.76\mu^2\mu_0^2}{\tau^3}e^x, \tag{26}$$

which extends the applicability of the analytic solutions down to $\tau > 5$. They showed that the error of the approximate solutions of the reflection function for nadir measurements is mostly less than 5% for sun zenith angles smaller $75°$ in the visible and near-infrared range. Only for very large sun zenith angles the error increases up to 7% in the near-infrared range.

Although molecular and aerosol scattering can be easily taken into account, SACURA neglects all these processes because wavelengths 0.86 and 1.6 μm are used in the retrieval for optically thick clouds. Then Rayleigh scattering and aerosol contribution are of no importance.

## 2.4. NASA MOD06 look-up table approach

The third retrieval used in this comparison was developed in the framework of the NASA EOS mission (King and Greenstone, 1999b) and is part of the MODIS MOD06 product. The LUT-based approach (King et al., 1997; Platnick et al., 2003) is similar to the ATSK3 retrieval but instead of channel 1, one of channels 1 (0.65 μm), 2 (0.86 μm) or 3 (1.2 μm) with respect to the minimization of the reflection from the underlying surface (land, ocean, ice) is chosen to retrieve the optical thickness and the effective radius is retrieved for each of the three absorbing channels 6 (1.6 μm), 7 (2.1 μm) and 20 (3.7 μm). For thick clouds, Eq. (7) is used. For the background albedo, data from the MODIS ground product MOD43 (Lucht et al., 2000) providing 16-day average datasets is used. The atmospheric correction is based on LUTs computed by MODTRAN 4 (Berk et al., 1998) and the MOD35 cloud mask product (Ackerman et al., 1998) is used to identify 100% overcast pixels that are considered for the retrieval and the cloud phase is derived from several NIR and IR bands (see Platnick et al., 2003 for details). An overview of MODIS channels used is given in Table 2.

Table 2
MODIS channels used in the retrievals

| Retrieval | Non-absorbing channel (μm) | Absorbing channel (μm) |
|---|---|---|
| ATSK3 | 0.65 | 3.7 |
| MOD06-16 | 0.65 over land and | 1.6 |
|  | 0.86 over ocean |  |
| MOD06-37 | 0.65 over land and | 3.7 |
|  | 0.86 over ocean |  |
| SACURA | 0.86 | 1.6 |

The MOD06 product was chosen as third retrieval for this comparison because of the three available effective radius products since a direct comparison of ATSK3 and SACURA would be complicated by the different penetration depth of the absorbing wavelengths at 1.6 μm and 3.7 μm into the cloud (Platnick, 2000; Kohanovsky, 2004d). In contrast to ATSK3 and SACURA results, which were processed by the authors within the LCRS operational processing scheme (Nauss and Bendix, in press), the already computed MOD06 product was supplied by NASA's Distributed Active Archive Center (DAAC, http://www.daac.gsfc.nasa.gov/).

## 3. Intercomparison of ATSK3, SACURA and MOD06

For the comparison, a scene over the Pacific ocean and one over central Europe are studied. The Pacific ocean scene minimizes the influence of the auxiliary data because the
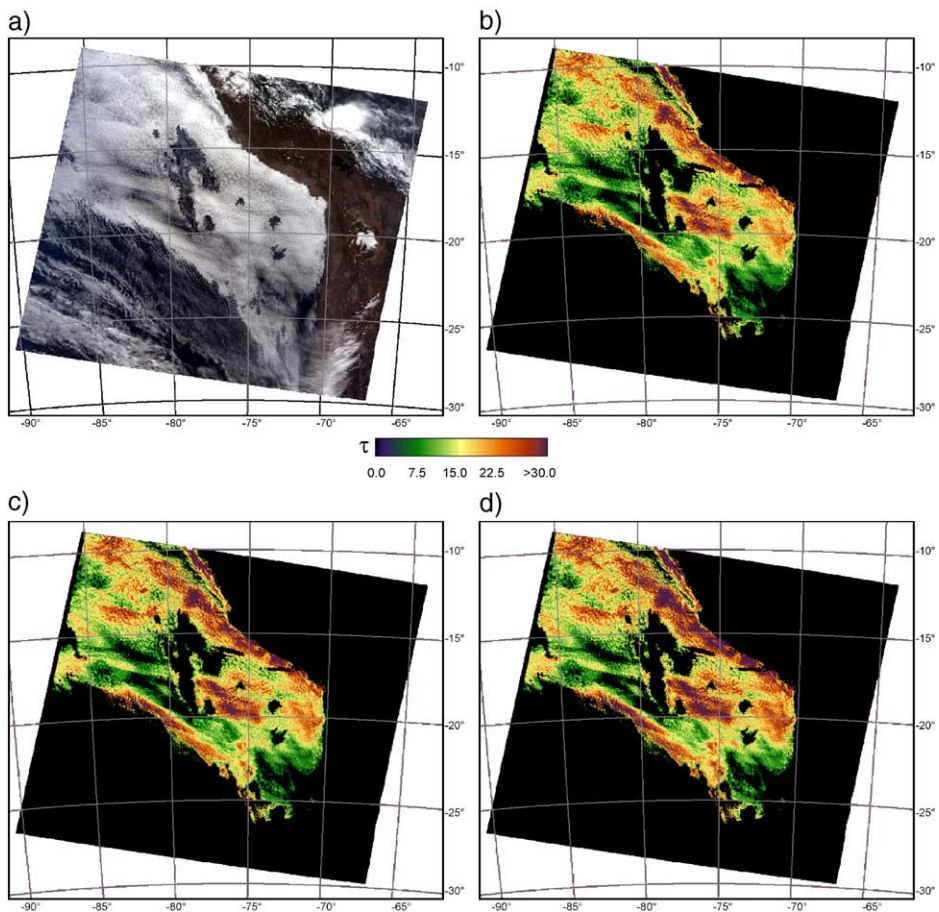


Fig. 2. Composite image (a) and optical thickness retrieved from MOD06 (b), ATSK3 (c) and SACURA (d) for Terra-MODIS scene from July 18th 2001, 15:30 UTC.

ocean background albedo is quite homogeneous and well known while the central Europe scene emphasizes the contribution of these data on the resulting parameters. Therefore, the resulting differences from the two scenes can be interpreted as the minimum and maximum stretch someone has to expect when using different retrieval techniques.

### 3.1. The Pacific ocean scene

For the ocean scene the same Terra-MODIS granule from July 18th 2001, 15:30 UTC (Fig. 2a) over the west coast of South America and adjacent Pacific areas as published by Platnick et al. (2003) was used. The areas in Fig. 2b–d show the field of marine stratocumulus clouds with an optical thickness larger than 5 in all three retrievals that are taken into account leading to a test sample of over 950,000 pixels each with a resolution of 1 km². Clouds over land are not considered for the retrieval since the influence of auxiliary data should be minimized for this comparison. For an overview of statistical values, see Table 3.

The optical thickness retrieved by the three techniques is shown in Fig. 2b–d with values from 5 to about 70 for ATSK3 and MOD06 and some isolated values up to 79 for SACURA. Note that $\tau$ retrieved by ATSK3 at 0.65 $\mu$m was converted to corresponding $\tau$ at 0.86 $\mu$m using the conversion function from Kokhanovsky et al. (2004) mentioned

Table 3
Comparison of ATSK3, SACURA and MOD 03 for the Terra-MODIS scene from July 18th 2001, 15:30 UTC

| Optical thickness (0.86 $\mu$m) | ATSK3 | SACURA | MOD06 |
|---|---|---|---|
| Min | 5.00 (10.00) | 5.00 (10.11) | 5.00 (10.00) |
| 1. Quartile | 11.36 (13.95) | 12.46 (15.34) | 10.80 (13.33) |
| Median | 15.75 (17.68) | 17.18 (19.31) | 14.92 (16.75) |
| 3. Quartile | 21.22 (22.86) | 23.06 (24.72) | 19.95 (21.34) |
| Max | 69.43 (69.43) | 78.77 (78.77) | 72.34 (72.34) |
| Mode | 13.70 (13.70) | 15.00 (15.00) | 12.30 (12.30) |
| Mean | 16.89 (19.10) | 18.47 (20.85) | 15.92 (17.98) |
| Standard deviation | 7.38 (6.62) | 7.99 (7.19) | 6.75 (6.01) |
| $r^2$ vs. MOD06 | 0.99 (0.99) | 0.99 (0.99) | |

| Effective radius | ATSK3 | MOD06-37 | SACURA | MOD06-16 |
|---|---|---|---|---|
| Min | 4.90 (4.90) | 5.09 (5.09) | 4.15 (4.24) | 4.45 (4.45) |
| 1. Quartile | 9.69 (9.60) | 9.22 (9.08) | 8.96 (8.89) | 8.75 (8.74) |
| Median | 11.74 (12.03) | 11.76 (11.91) | 10.06 (10.03) | 9.95 (10.02) |
| 3. Quartile | 13.65 (13.86) | 13.81 (14.00) | 11.81 (11.71) | 11.96 (12.11) |
| Max | 23.56 (22.24) | 30.00 (30.00) | 24.15 (19.96) | 30.00 (23.95) |
| Mode | 9.00 (9.30) | 8.90 (8.90) | 9.60 (9.60) | 8.90 (8.90) |
| Mean | 11.83 (11.92) | 11.83 (11.82) | 10.61 (10.50) | 10.61 (10.63) |
| Standard deviation | 2.42 (2.45) | 2.84 (2.83) | 2.41 (2.26) | 2.63 (2.53) |
| $r^2$ vs. MOD06 | 0.97 (0.99) | | 0.91 (0.94) | |

Values for optical thickness are valid for 0.86 $\mu$m and values of the effective droplet radius are retrieved using the 1.6-$\mu$m (SACURA, MOD06-16) and 3.7-$\mu$m (ATSK3 and MOD06-37) channels. First ($Q_1$) (third ($Q_3$)) quartile represents values of the random parameter $X$ for which 25% (75%) of observations give values of $X$ smaller than $Q_1$ ($Q_3$). Values in brackets represent results for $\tau \geq 10$.

above. The thickest clouds can be found along the coast of Peru, in the centre of the scene and along the south-western border of the cloud field. In the centre, the small scale inhomogeneities (10 km to 30 km across) of the mesoscale cellular convection cumulus cloud tops, further accentuated by the mentioned 3-D radiation effects can be clearly identified.

The mean optical thickness of 15.9 (MOD06), 16.9 (ATSK3) and 18.5 (SACURA) and the standard deviations are laying within 6% to 18% reasonably close to each other. As can be also seen in Fig. 3, all three distribution functions have a positive skewness with mode values of 12.3 (MOD06), 13.7 (ATSK3) and 15.0 (SACURA) showing slightly larger deviations up to 22% but the solutions of ATSK3 and SACURA reveal still a clear positive correlation with the ones of MOD06 (Fig. 4a,b) with an identical stability index $r^2$ of 0.99. However, an obvious deviation for both products towards larger $\tau$ is present which is also evident in Fig. 4c,d. Compared to MOD06 the ATSK3 results differ by no more than 20%. The spread is decreasing with increasing $\tau$ and the deviation is limited to +5% to +15% for $\tau > 32$.

Variation of SACURA is generally larger. For $\tau < 10$ differences of more than 50% occur declining to generally less than 25% for $\tau > 15$. Like for ATSK3, the spread decreases with increasing $\tau$ staying mainly within +10% to +25%. Whether the positive deviation of SACURA and ATSK3 is an indication for an underestimation of $\tau$ by MOD06 in this case is not clear.

Fig. 5 shows the spatial distribution of the deviation of $\tau$. While comprehensive regions of the SACURA (b) as well as the western part of the ATSK3 results (a) differ by 5% to 25%, the latter shows a predominate agreement within $\pm 5\%$ in the eastern part. Only along the borders of the enclosed patches of open cells (POCs, see Bretherton et al., 2004) the deviation of SACURA reaches up to 30% (presumably caused by different responses of the algorithms to enhanced 3-D radiation effects and drizzle) .

The retrieved effective cloud droplet radii are shown in Fig. 6. As already mentioned significantly different spectral bands have been used for the comparison of the effective
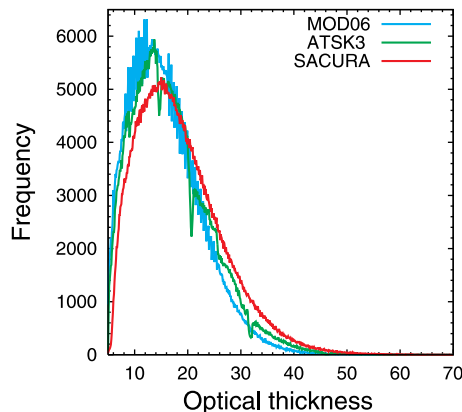


Fig. 3. Distribution functions of optical thickness retrieved by MOD06, ATSK3 and SACURA for Terra-MODIS scene from Fig. 2.
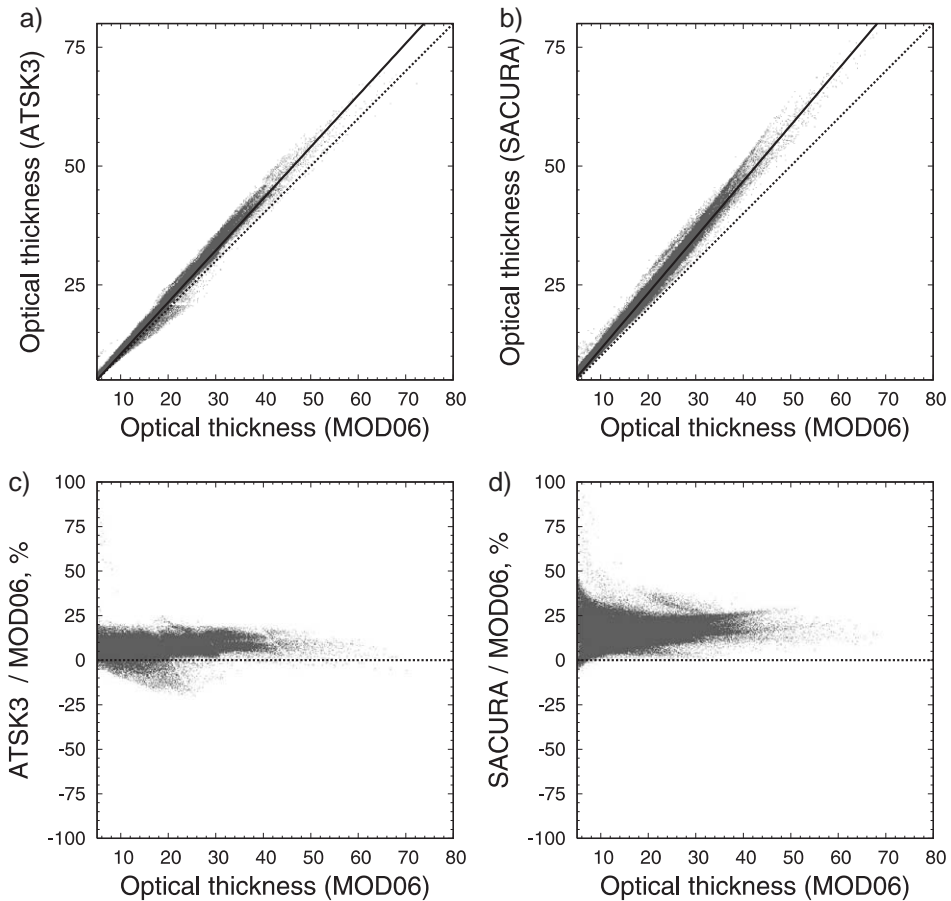
Fig. 4. Optical thickness retrieved by ATSK3 (a) and SACURA (b) vs. MOD06 and corresponding percentage difference (c, d) for Terra-MODIS scene from Fig. 2.

radius. Therefore the 1.6-μm-based effective radius of MOD06 (further referred as MOD06-16) has been taken into account for SACURA while for ATSK3 the 3.7-μm-based MOD06 product (further referred as MOD06-37) has been used.

Minimum values of $a_{ef}$ are between 4.2 μm and 5.1 μm, maximum values range from 23.7 μm (ATSK3) over 24.2 μm (SACURA) up to 30 μm (MOD06-16 and MOD06-37). As for τ the largest $a_{ef}$ can be found south-west of an about 200-km-wide band along the coast and at the southern border. The large $a_{ef}$ around the POCs can be likely traced back to a combination of enhanced 3-D effects, subpixel cloudiness and drizzle. The different penetration depths of ATSK3 and SACURA are most apparent in the eastern cloudy region but the low optical thickness values as well as the composite image (Fig. 2)) indicate that in the very south-eastern part of this region, the effective radius is artificially increased by less dense cellular convection leading to an increasing number of only partially filled cloudy pixels. Nevertheless there is in general a positive correlation of band-dependent
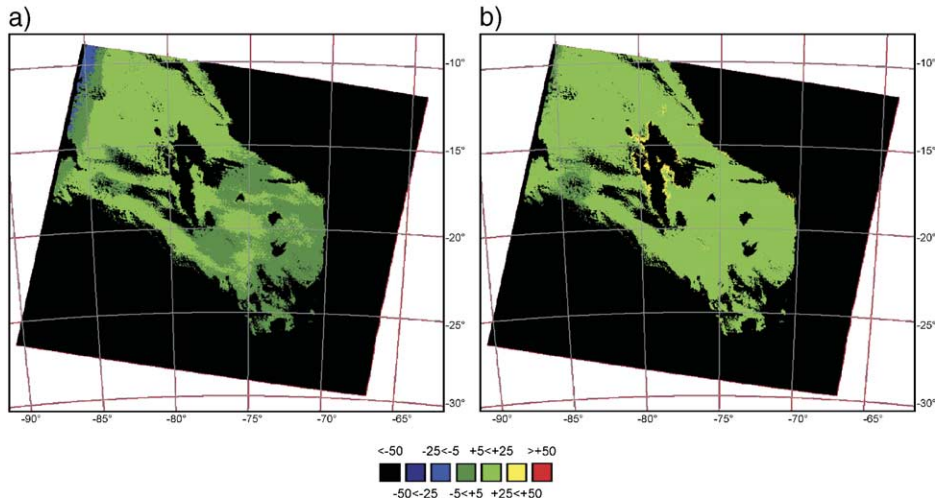
Fig. 5. Spatial distribution of the percentage deviation of cloud optical thickness between MOD06 and ATSK3 (a) and SACURA (b), respectively, for Terra-MODIS scene from Fig. 2.

retrieval level inside the cloud and particle size. This is also evident in the mean and median values (see Table 3) which are about 11% to 18% larger for ATSK3 and MOD06-37 as for SACURA and MOD06-16. The differences in standard deviations in all 4 products are small.

It can be seen in Fig. 7a,c that the ATSK3 retrieved values are larger for $a_{ef} < 8.0$ μm but smaller for $a_{ef} > 16.5$ μm and in general the deviation is within $\pm 10\%$. The maximum bias increase for some pixels with large $a_{ef}$ up to 35%. Similar but less compact tendencies can be found for SACURA (Fig. 7b,d). The majority of the retrieved values match by $\pm 10\%$ but for $a_{ef} < 13$ μm deviation increases up to about +25%. and negative bias of the same magnitude can be found for some pixels with $a_{ef} > 20$ μm.

The scatter plots of ATSK3 vs. MOD06-37 (Fig. 7a) and SACURA vs. MOD06-16 (Fig. 7b), respectively, show similar tendencies ($r^2 = 0.97$ for ATSK3 and $r^2 = 0.91$ for SACURA) but the distribution functions are clearly different (Fig. 8). The 1.6-μm products show a unimodal, positive skewed distribution with mode around 9 μm while the 3.7-μm products have a bimodal distribution with the same mode but an additional local maximum at 13 μm. The 13-μm radii are mainly caused by convective processes concentrated in the medium to high dense cumulus regions north-west and south-east of the large central POC where optical thickness is commonly above 25. The feature cannot be seen in SACURA results because of the deeper depth of penetration inside the cloud where mixing processes have counterbalanced the intense cloud droplet growth in the upper most layer of the convective clouds.

As for $\tau$ (and in contrast to SACURA and ATSK3), the distribution functions of the NASA products show small scale but high frequent oscillations. The underlying reason behind these oscillations is not clear to us.

Fig. 9 shows that the majority of pixels differs by not more than $\pm 5\%$. In the ATSK3 results the largest spatially significant positive deviations of +5% to +25% found along the
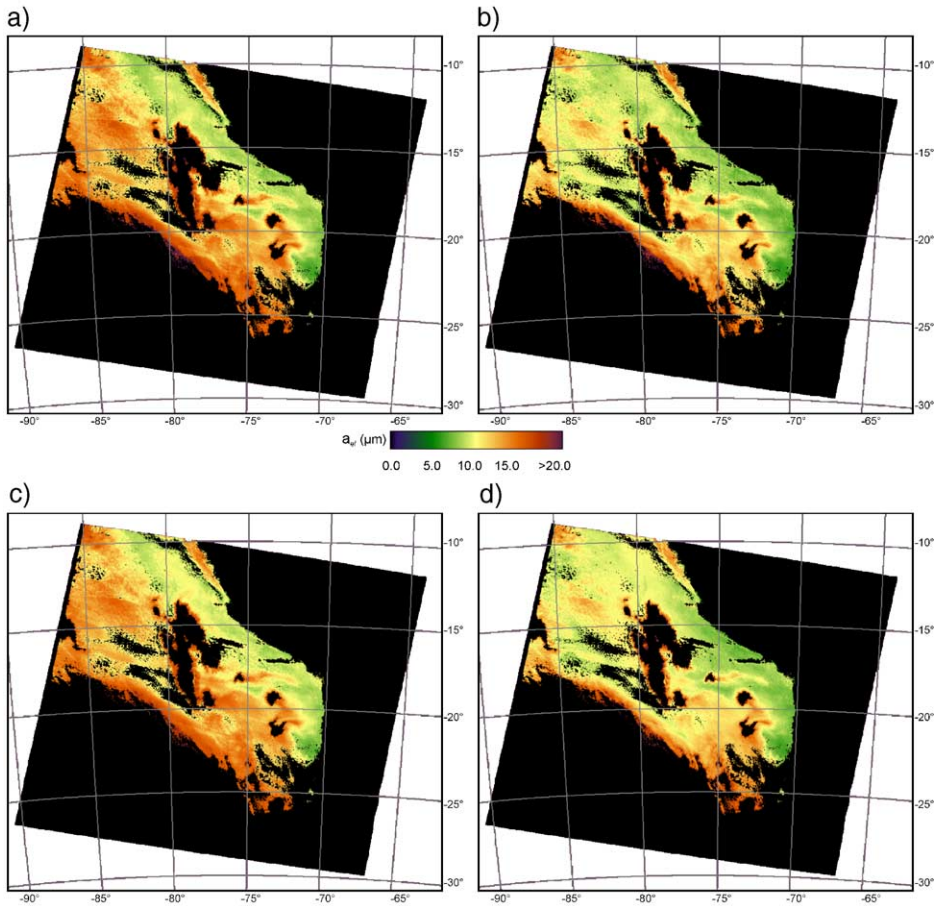
Fig. 6. Effective cloud droplet radius retrieved from MOD06-37 (a), MOD06-16 (b), ATSK3 (c) and SACURA (d) for Terra-MODIS scene from Fig. 2.

mentioned coastal band and the largest negative deviations of the same magnitude are located in some limited areas in the south. SACURA has the largest bias of up to $-25\%$ in the central cloud field and along the southern central cloud border. Regional positive deviations can be found in the north-western and south-eastern area.

If only pixels with $\tau > 10$ are taken into account, the bias between the retrievals decreases. Corresponding statistics can be found in the brackets of Table 3.

The coherence between the derived liquid water path (see Eq. (21)) can be seen in Figs. 10 and 11. As expected with regard to the results presented above, the bias increases slightly with increasing LWP but deviations for LWP $> 100$ g/m$^2$ are in general within $-5\%$ to $+15\%$ for ATSK3 and $+20\%$ for SACURA. The resulting $r^2$ is 0.98 for both ATSK3 and SACURA.

In summary, the values of $a_{ef}$ are larger for the wavelength 3.7 μm (by approximately 1 μm on average). This is best explained by the decrease of the droplet size from top to the
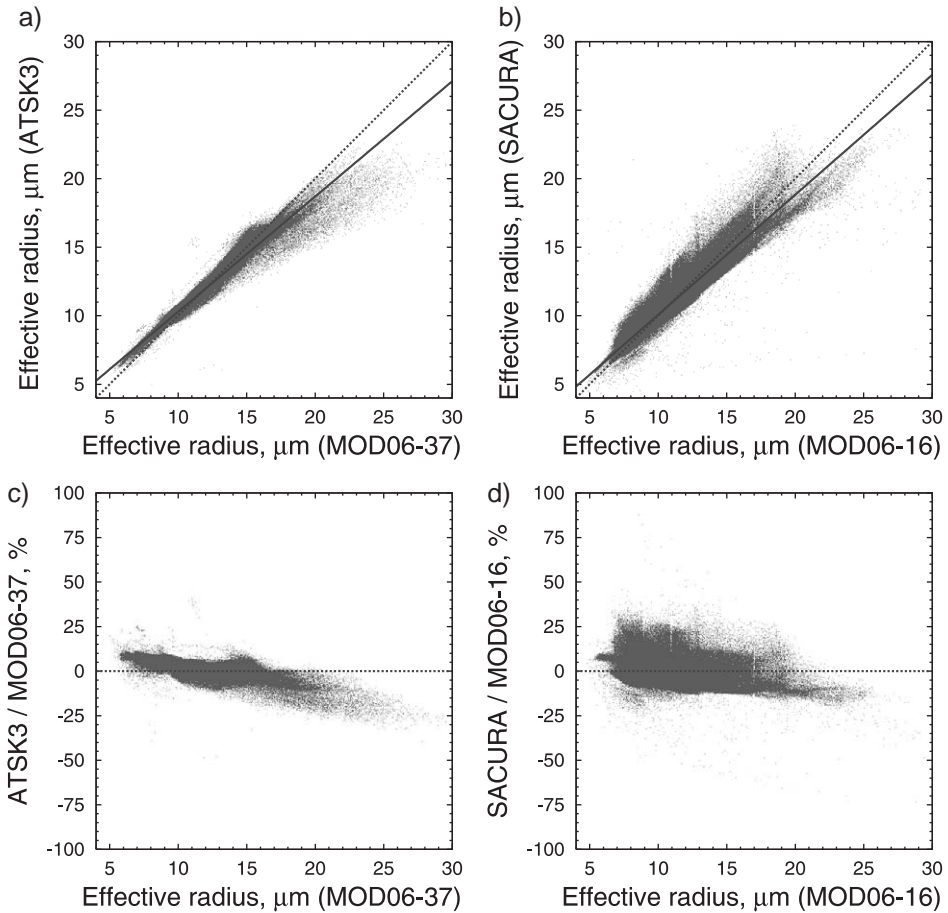
Fig. 7. Effective cloud droplet radius retrieved by ATSK3 (a) and SACURA (b) vs. MOD06-37 and MOD06-16, respectively, and corresponding percentage difference (c, d) for Terra-MODIS scene from Fig. 2.

bottom. Mean effective radii retrieved by SACURA and those from MOD06-16 are identical and almost coincide for MOD06-37 and ATSK3. Mean cloud optical thickness is in the range 16–18.5 from all these retrievals. So we see that all techniques reproduce average cloud microphysical properties in a similar way. The situation is much more complicated over land, where there is an important contribution from the ground surface. This case will be considered in the next section.

## 3.2. The central Europe scene

Fig. 12a shows the composite image for the Terra-MODIS scene from August 10th 2002, 9:45 UTC over Germany. The complex cloud structures are induced by large scale labialization due to a low pressure system over France leading to intensive showers over
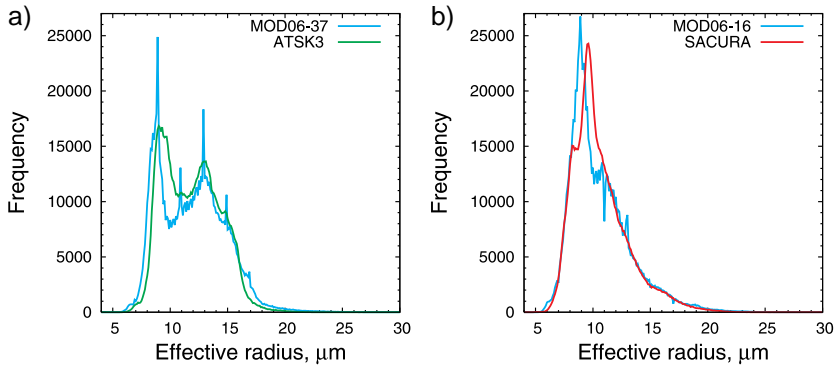
Fig. 8. Distribution functions of effective cloud droplet radius retrieved by ATSK3 (a), SACURA (b) as well as corresponding MOD06-37 and MOD06-16 values for Terra-MODIS scene from Fig. 2.

southern Germany during the extreme flooding events over central Europe in August 2002. In contrast to the Pacific scene, MOD06 uses the 0.65-µm channel over land surfaces so that this time $\tau$ retrieved by SACURA at 0.86 µm was converted to corresponding $\tau$ at 0.65 µm using again the conversion function from Kokhanovsky et al. (2004). Ice phase cumulus cloud clusters in the southern and north western part are excluded from the comparison and once again, only clouds with $\tau > 5$ are taken into account. The resulting area can be seen in the images of retrieved $\tau$ values from MOD06 (Fig. 12b), ATSK3 (Fig. 12c) and SACURA (Fig. 12d).
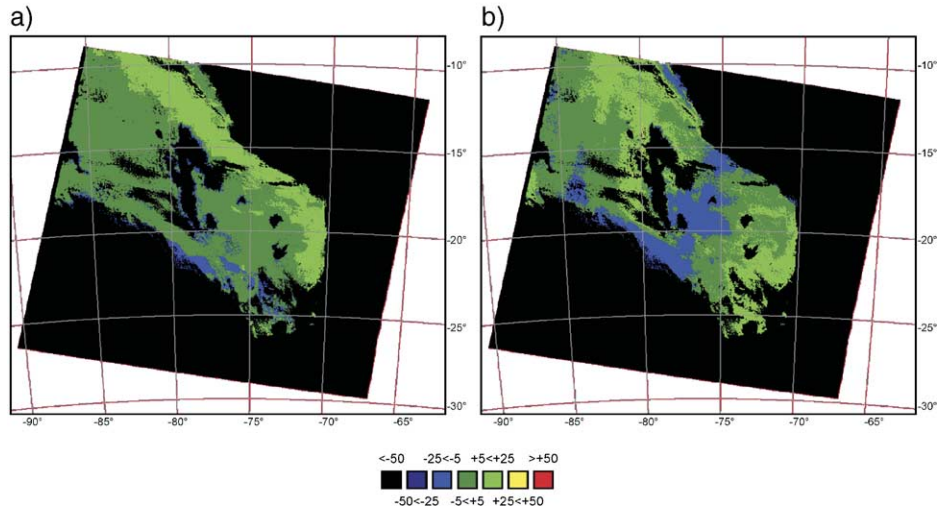


Fig. 9. Spatial distribution of the percentage deviation of cloud effective droplet radius between MOD06-37 and ATSK3 (a) and MOD06-16 and SACURA (b) for Terra-MODIS scene from Fig. 2.
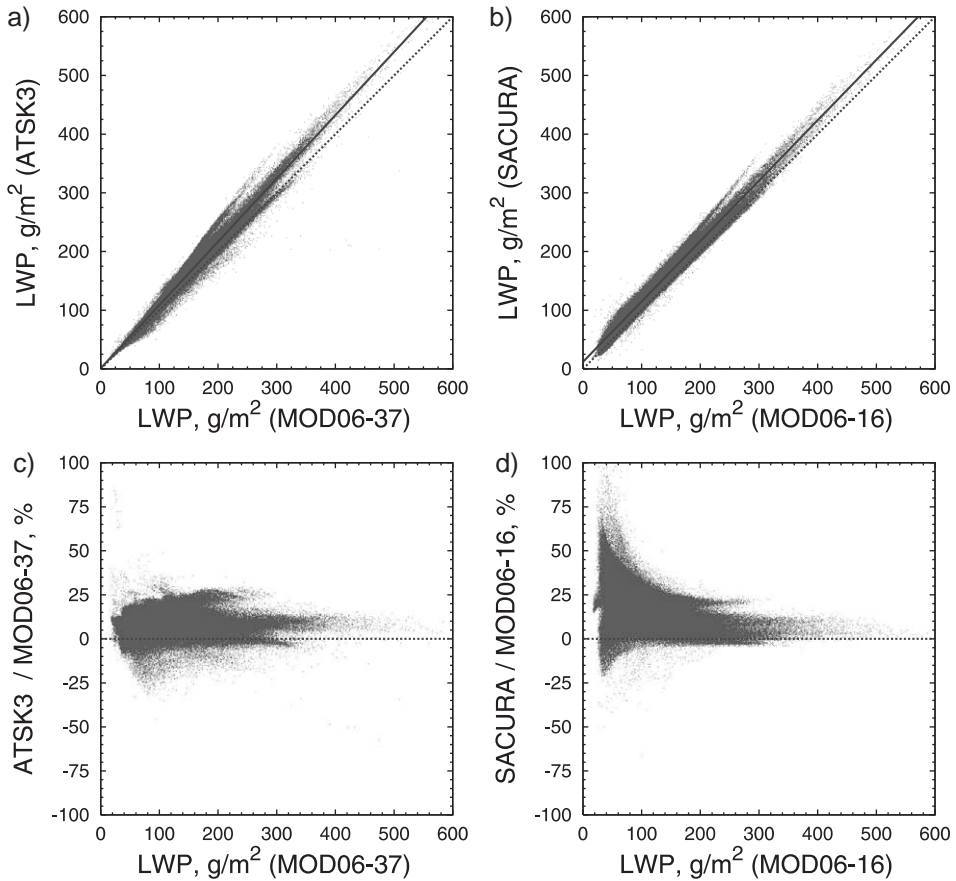
Fig. 10. Liquid water path retrieved by ATSK3 (a) and SACURA (b) vs. MOD06 and corresponding percentage difference (c, d) for Terra-MODIS scene from Fig. 2.

The overall pattern is very similar for all retrievals with optically thin, low stratus clouds surrounded by dense cumulus clouds with $\tau$ larger 30 and up to 70 or 80 (not distinguishable on the scale) in the regions around. All three retrievals show good positive correlations (Fig. 13a,b) with $r^2$ between 0.95 (SACURA) and 0.98 (ATSK3) but in general, $\tau$ values from ATSK3 and especially SACURA are higher than corresponding MOD06 results (Table 4). This can be also seen in Fig. 14 with a mode value of 11.2 for SACURA while the maximum number of pixels for MOD06 is found for $\tau = 9$. A similar percentage difference is found between the mean values of SACURA and MOD06. The skewness in SACURA is generally larger than in ATSK3 but majority of deviations lies within a 20% range between +10% and +30%. A striking feature can be seen in Fig. 14a and c with two clearly distinguishable scatter tendencies of ATSK3. While the majority of pixels is within a −5% to +10% border, a second deviation pattern especially for $\tau < 30$ with differences between 25% and 70% is present. As it can
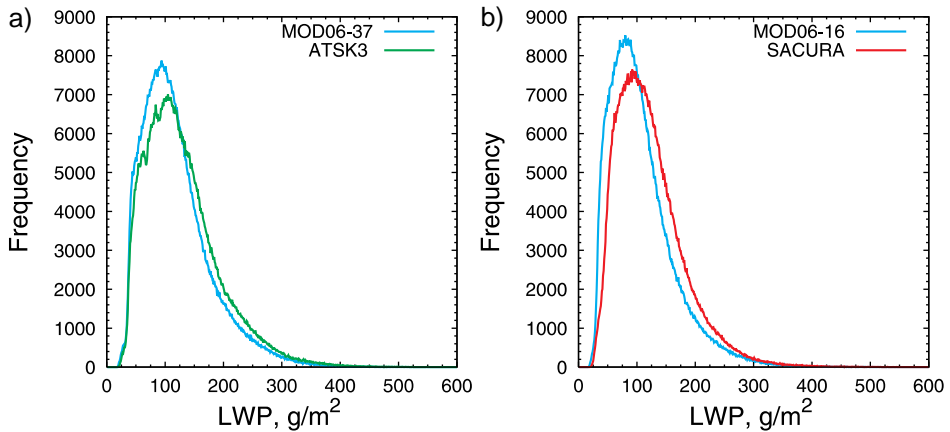
Fig. 11. Distribution functions of liquid water path retrieved by MOD06, ATSK3 and SACURA for Terra-MODIS scene from Fig. 2.

be seen in Fig. 15a these deviations are mainly located at the southern end of the conveyor belt like feature building a south-eastern extension to the northern cumulus cloud clusters. As for the entire scene, cloud inhomogeneity is significant and different responses of the algorithms to 3-D radiation effects may be responsible for many of these deviations.

The distribution of $a_{ef}$ (Fig. 16) is as expected with low to medium values in the stratiform areas and increasing values at the conveyor belt like feature as well as towards the deep convective cloud clusters. In contrast to the non-precipitating ocean scene the values retrieved at 1.6 μm are larger than the corresponding 3.7-μm values mainly due to growing precipitation particles within deeper cloud layers increasing the 1.6-μm $a_{ef}$ values (Rosenfeld et al., 2004).

In contrast to $\tau$, the retrieved $a_{ef}$ from SACURA shows no general tendency for overestimation (Fig. 17b,c) and the majority of pixels from both retrievals differ by no more than ±10% although the skewness is much larger for SACURA than for ATSK3. The distinct bias exception for ATSK3 retrieved at $a_{ef} < 12$ μm (Fig. 17a) corresponds to the above-mentioned bias of $\tau$. Besides the mentioned 3-D effects and especially in this scene where only a limited number of cloud-free pixels for the ground temperature interpolation (see Section 3.1) is available, uncertainties in auxiliary datasets can cause such significant differences (see Section 5). From visual inspection a wrong classified thin cirrus overlay can be identified as a third contribution to the deviations. Especially the cirrus effect can be an explanation for the existence of the same feature in the $\tau$ and $a_{ef}$ retrieval. The coinciding locations can be seen in Figs. 15 and 19. Increased ice crystal absorption can reduce the 3.7-μm radiance and therefore increase an assumed value of $a_{ef}$. Beside this, the deviation between ATSK3 and MOD06-37 is mainly within −10% to +7%.

The large bias at 6.7 μm is caused by an artefact in both MOD06 retrievals as it can be seen in Fig. 18. The mode of the MOD06-37 retrieval at 6.7 μm is caused by
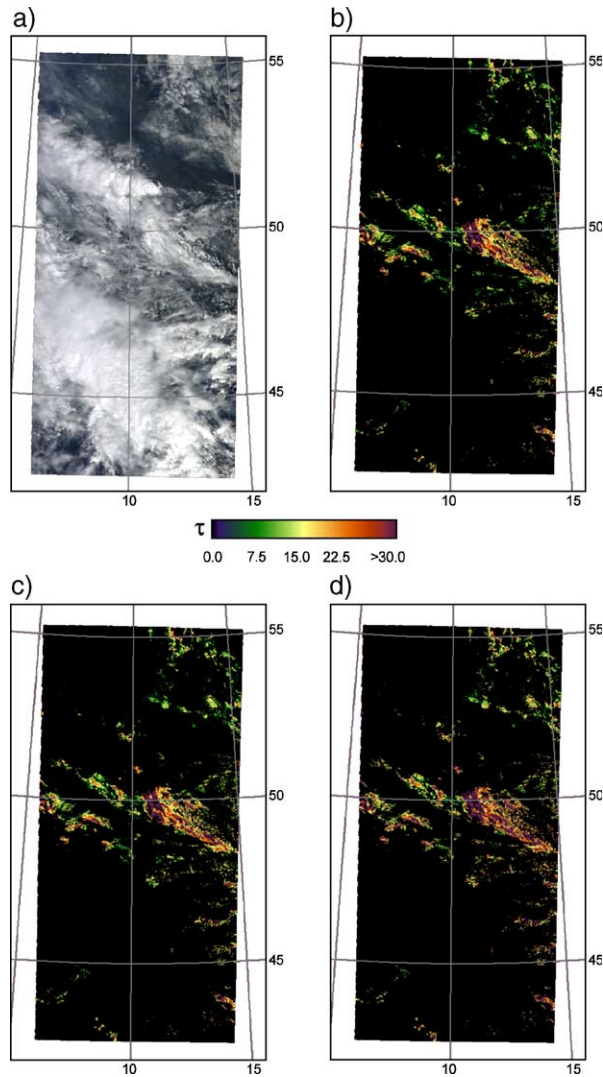
Fig. 12. Composite image (a) and optical thickness retrieved from MOD06 (b), ATSK3 (c) and SACURA (d) for Terra-MODIS scene from August 10th 2002, 09:45 UTC.

about 3483 pixels, which is about 250% above the amount of pixels found in the range of the ATSK3 mode value at 8.7 μm. The artefact in the MOD06-16 product is even further emphasized and is made up of about 7723 pixels. Neglecting values of 6.7 μm as it is done for the values in Table 4, $r^2$ increases from 0.46 to 0.60 for SACURA and from 0.67 to 0.84 for ATSK3. If again only pixels with $\tau > 10$ are taken into account the bias further decreases and $r^2$ further increases up to 0.79 for SACURA and 0.90 for ATSK3.
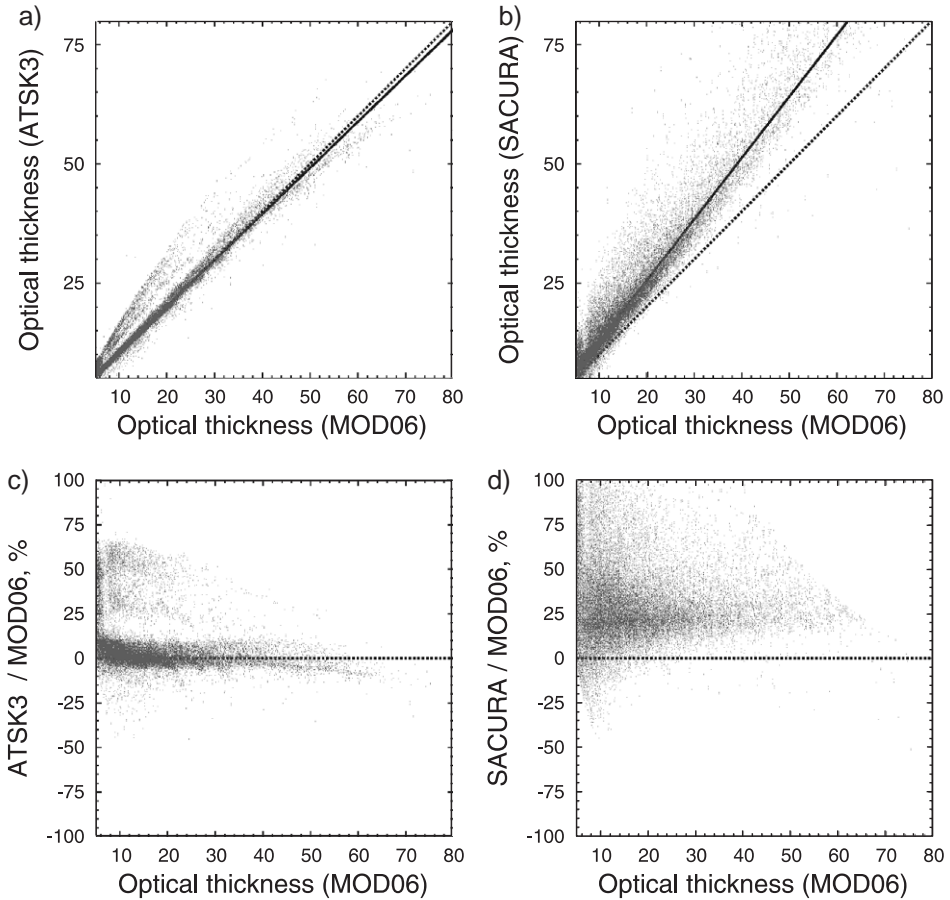
Fig. 13. Optical thickness retrieved by ATSK3 (a) and SACURA (b) vs. MOD06 and corresponding percentage difference (c, d) for Terra-MODIS scene from Fig. 12.

The coherence between the derived liquid water path (see Eq. (21)) is similar to Figs. 10 and 11 but since bias is increased for $\tau$ and $a_{ef}$, the resulting $r^2$ is 0.67 for SACURA and 0.86 for ATSK3.

## 4. Sensitivity of retrievals to auxiliary data

Different results for the ocean and land scenes found here cannot be induced by the numerical uncertainties of the algorithms itself. Naturally, the two scenes differ very much with regard to cloud-top inhomogeneities and the resulting more enhanced 3-D effects for the land scene will increase the differences between the retrievals but the increased influence of auxiliary data uncertainties should be taken into account, too. Over sea, ground albedo is usually small and both ground albedo and ground temperature are quite

Table 4
Comparison of ATSK3, SACURA and MOD03 for the Terra-MODIS scene from August 10th 2002, 09:45 UTC

| Optical thickness (0.65 μm) | ATSK3 | SACURA | MOD06 | |
|---|---|---|---|---|
| Min | 5.00 (10.00) | 5.00 (10.00) | 5.00 (10.00) | |
| 1. Quartile | 9.94 (13.73) | 12.00 (17.13) | 9.64 (13.64) | |
| Median | 14.63 (18.69) | 18.40 (23.48) | 14.47 (18.58) | |
| 3. Quartile | 23.23 (27.24) | 29.19 (34.60) | 22.97 (27.04) | |
| Max | 69.84 (69.84) | 80.00 (80.00) | 79.39 (79.39) | |
| Mode | 8.90 (13.70) | 11.20 (15.00) | 9.00 (12.30) | |
| Mean | 18.21 (22.12) | 22.97 (28.15) | 18.04 (22.04) | |
| Standard deviation | 11.19 (10.89) | 15.15 (14.84) | 11.46 (11.15) | |
| $r^2$ vs. MOD06 | 0.98 (0.98) | 0.95 (0.93) | | |

| Effective radius | ATSK3 | MOD06-37 | SACURA | MOD06-16 |
|---|---|---|---|---|
| Min | 4.11 (4.11) | 4.55 (4.55) | 4.06 (4.13) | 4.00 (4.00) |
| 1. Quartile | 7.99 (7.65) | 8.44 (8.07) | 9.62 (9.17) | 9.16 (8.80) |
| Median | 9.54 (9.14) | 9.87 (9.47) | 12.81 (11.78) | 12.05 (11.17) |
| 3. Quartile | 11.41 (11.05) | 11.44 (11.18) | 17.75 (15.88) | 16.57 (14.65) |
| Max | 27.47 (27.09) | 30.00 (21.65) | 30.00 (29.99) | 30.00 (30.00) |
| Mode | 8.70 (9.30) | 10.90 (8.90) | 8.80 (8.80) | 9.00 (9.00) |
| Mean | 9.93 (9.59) | 10.13 (9.82) | 14.18 (13.08) | 13.39 (12.23) |
| Standard deviation | 2.65 (2.65) | 2.34 (2.36) | 5.67 (5.05) | 5.50 (4.64) |
| $r^2$ vs. MOD06 | 0.84 (0.90) | | 0.60 (0.79) | |

Values for optical thickness are valid for 0.65 μm and values of the effective droplet radius are retrieved using the 1.6-μm (SACURA, MOD06-16) and 3.7-μm (ATSK3 and MOD06-37) channels. First ($Q_1$) (third ($Q_3$)) quartile represents values of the random parameter $X$ for which 25% (75%) of observations give values of $X$ smaller than $Q_1$ ($Q_3$). Values in brackets represent results for $\tau \geq 10$. Pixels with $a_{ef} = 6.7$ μm are not considered (see text for details).

homogeneous. So especially the latter can be determined with high accuracy from cloud-free regions. This is not the case over land and especially for the cloudy scene chosen in Fig. 12. To estimate the influence of auxiliary data retrieved under operational conditions, a test sample of randomly chosen pixels with values of $a_{ef}$ of 8 μm and 16 μm and values
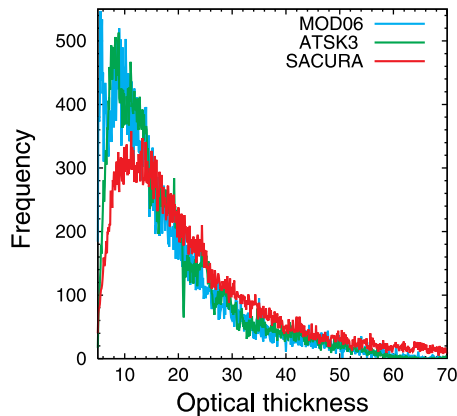


Fig. 14. Distribution functions of optical thickness retrieved by MOD06, ATSK3 and SACURA for Terra-MODIS scene from Fig. 12.
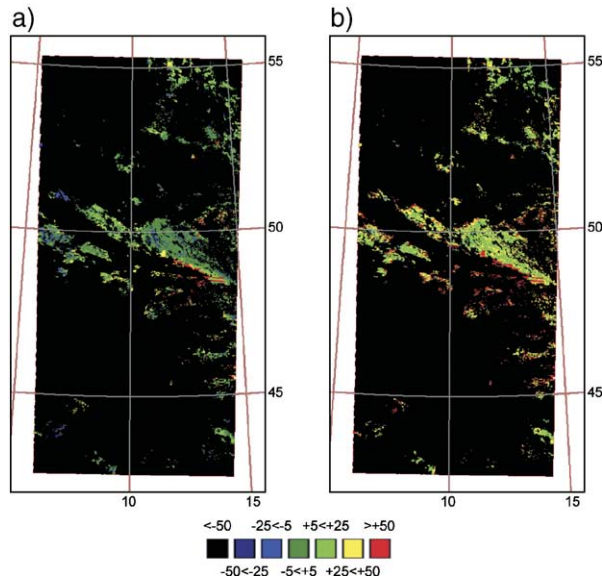
Fig. 15. Spatial distribution of the percentage deviation of cloud optical thickness between MOD06 and ATSK3 (a) and SACURA (b), respectively, for Terra-MODIS scene from Fig. 12.

of $\tau$ ranging from 5 to 30 in steps of 5 is selected from the MODIS scene shown in Fig. 11 and the values of one auxiliary datasets at a time are changed by $\pm 30\%$.

Fig. 19 shows the influence of ground albedo maps on retrieved parameters of ATSK3. Differences between $\pm 30\%$ in non-absorbing and absorbing band ground albedo have only a weak influence on the retrieved $\tau$ never exceeding 5% deviation. The differences in $\tau$ are due to an assumed larger (smaller) proportion of the cloud signal in the measured radiances when ground albedo decreases (increases). This leads to larger (smaller) values of $\tau$. For $a_{ef}$, slightly increasing values caused by decreasing near-infrared ground albedo are also negligible but the deviations caused by the visible ground albedo cannot be explained by the characteristics of the reflection functions alone. If absorbing channel cloud reflection is fixed and assumed non-absorbing channel reflection signal decreases caused by increasing ground albedo then $a_{ef}$ should decrease, too, and vice versa. While most samples show an increase in resulting $a_{ef}$ values for negative deviations of non-absorbing ground albedo, only a few show the assumed decrease for positive albedo deviations. This might be caused by the concept of the LUT retrieval where the iteration for different values of $\tau$ and $a_{ef}$ is halted as soon as the difference between measured and calculated signal is below a specified threshold value. Therefore a less likely combination of $\tau$ and $a_{ef}$ can be found under these circumstances where ground albedo of one channel is artificially modified. The clearly increased deviations between 10% and 20% for large $\tau$ and $a_{ef}$ should not be overrated. These combinations are not very common (Nakajima and Nakajima, 1995) and should be regarded as not representative for the performance of the retrieval. Actually, SACURA can be used as a subroutine of more general LUT-based approaches to deal with such complex retrieval situations or as a generator of a first guess retrieval, which could be refined at later stages.
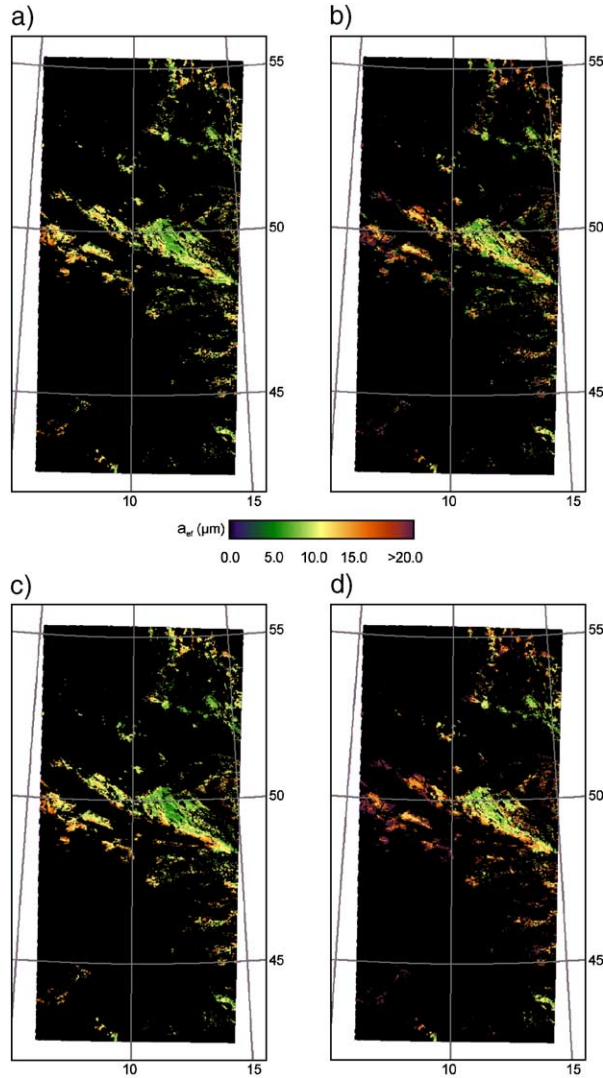
Fig. 16. Effective cloud droplet radius retrieved from MOD06-37 (a), MOD06-16 (b), ATSK3 (c) and SACURA (d) for Terra-MODIS scene from Fig. 12.

The sensitivity to other necessary auxiliary datasets of vertical humidity profile and ground temperature are shown in Fig. 20. While the vertical humidity profile has no influence on $\tau$ and only a weak influence of in general less than 4% on $a_{ef}$, ground temperature is crucial especially for the droplet size retrieval. The majority of samples shows the expected increase in $a_{ef}$ with increasing ground temperature since the latter results in a decreased cloud radiation signal and therefore increased values of $a_{ef}$ (see Fig. 1). But similar to Fig. 21c, the pixels with large values of $a_{ef}$ and $\tau$ show a different behaviour.
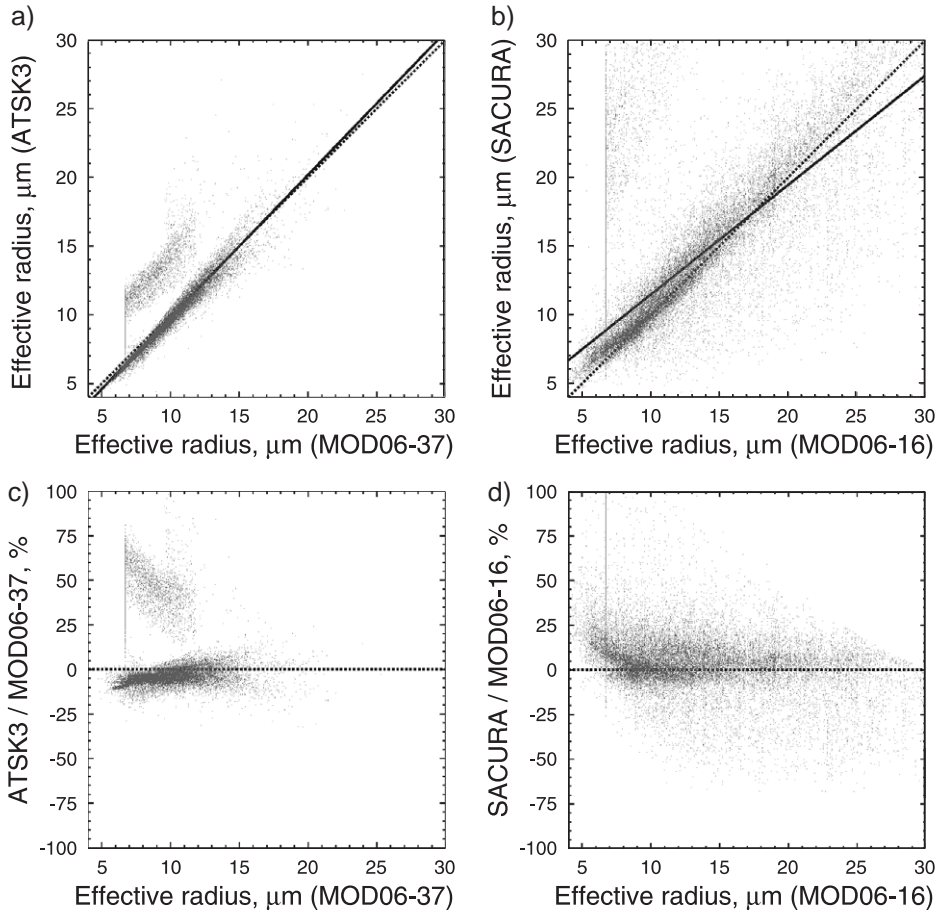
Fig. 17. Effective cloud droplet radius retrieved by ATSK3 (a) and SACURA (b) vs. MOD06-37 and MOD06-16, respectively, and corresponding percentage difference (c, d) for Terra-MODIS scene from Fig. 12.

Fig. 22 shows the sensitivity of SACURA to ground albedo changes. As expected the absolute influence of uncertainties in the non-absorbing channel ground albedo is higher over land areas for the 0.86-μm non-absorbing band used by SACURA than the 0.65-μm band used by ATSK3 and MOD06 (Platnick et al., 2003). It should be stressed that the mean ground albedo of the pixels used for this sensitivity study was about 0.10 at 0.65 μm but about 0.30 to 0.40 at 0.86 μm. Therefore a change of ground albedo by ±30% corresponds to an absolute change in ground albedo of about ±0.03 at 0.65 μm but ±0.10 at 0.86 μm. The change of $\tau$ in Fig. 22 is therefore caused by much larger absolute changes in ground albedo. Nevertheless, the error increases from 0.65 μm to 0.86 μm since a change of ground albedo of 0.01 leads to a change of $\tau$ at 0.65 μm by about 1% to 1.5% while at 0.86 μm, $\tau$ changes by about 2%. This is in agreement with Kokhanovsky et al. (2003), where $\delta\tau/\delta A_g = 1/$
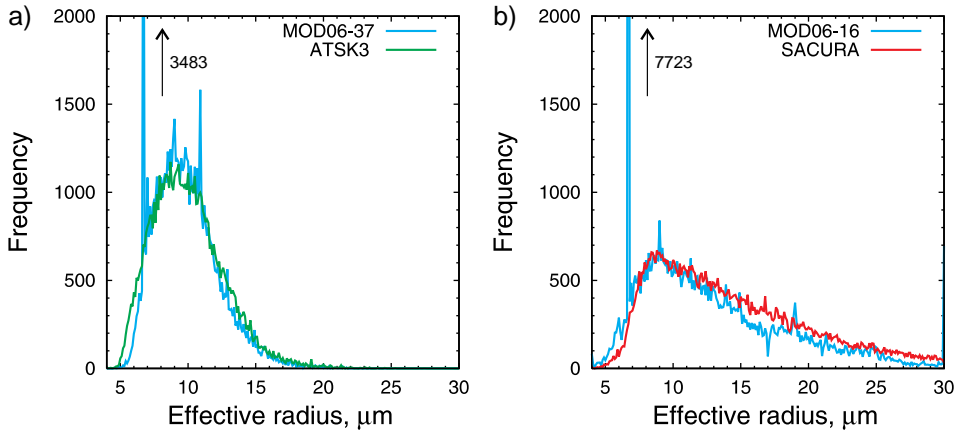
Fig. 18. Distribution functions of effective cloud droplet radius retrieved by ATSK3 (a), SACURA (b) as well as corresponding MOD06-37 and MOD06-16 values for Terra-MODIS scene from Fig. 12.

$0.75(1-g)(1-A_g)^2$ increases with increasing $A_g$. For $g=0.85$ the difference in $\tau$ is about 40% smaller for an average $A_g$ of 0.10 compared to an $A_g$ of 0.30 to 0.40.

In contrast to the behaviour of $a_{ef}$ in Fig. 21c, deviations of both $\tau$ and $a_{ef}$ within SACURA can be explained by the properties of the reflection function. If non-absorbing albedo increases (decreases), the cloud signal in Eq. (18) decreases
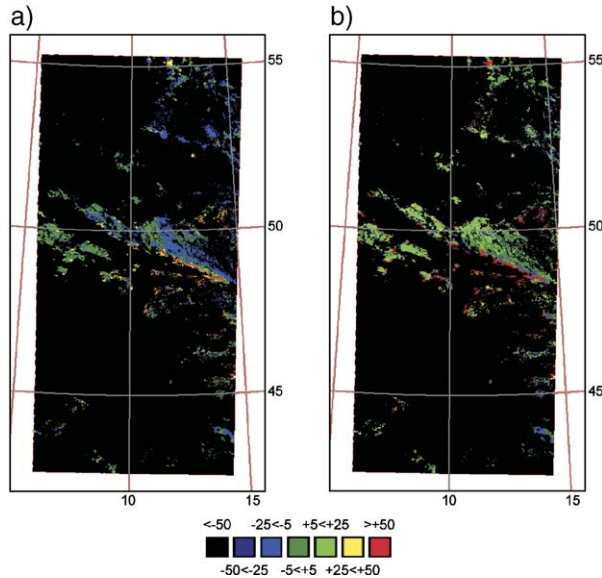


Fig. 19. Spatial distribution of the percentage deviation of cloud effective droplet radius between MOD06-37 and ATSK3 (a) and MOD06-16 and SACURA (b) for Terra-MODIS scene from Fig. 12.
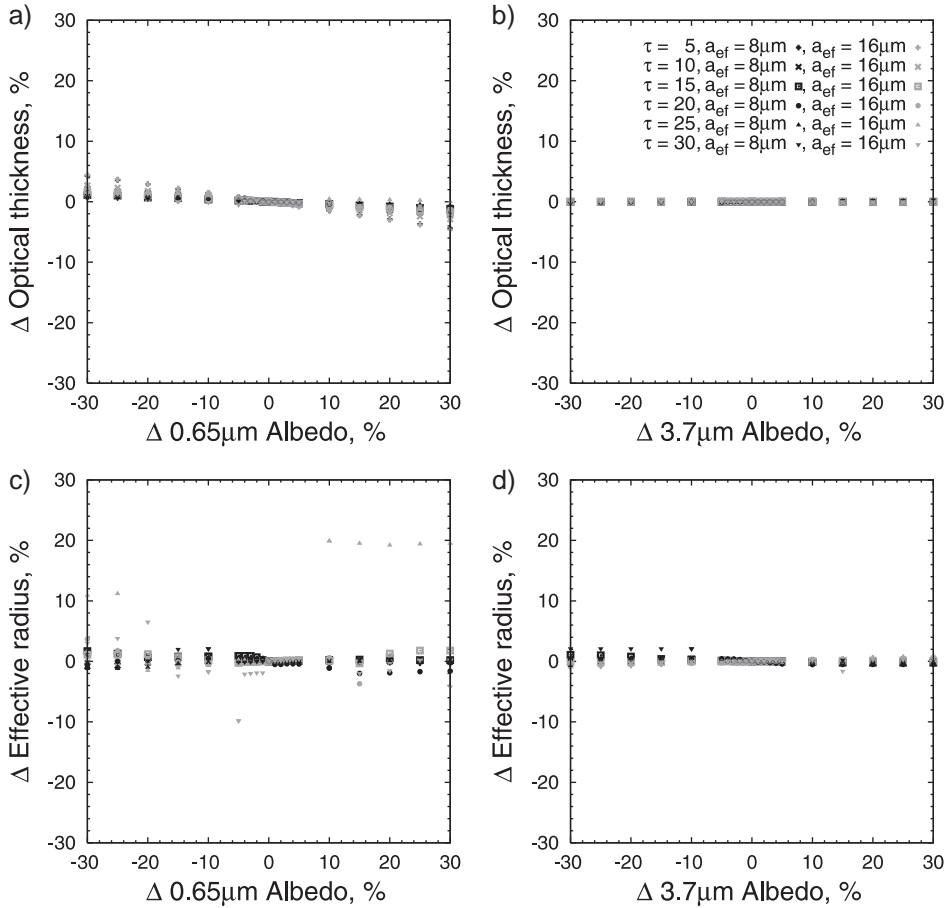
Fig. 20. Influence of errors in auxiliary ground albedo data for the non-absorbing (0.65 μm) and absorbing bands (3.7 μm) on the resulting optical thickness and effective cloud droplet radius of ATSK3 for $a_{\mathrm{ef}}$ values of 8 μm and 16 μm and 6 different values of t between 5 and 30. The pixels used for each class are randomly chosen from the Terra-MODIS scene from Fig. 12.

(increases) and therefore optical thickness decreases (increases), too. The same is true for $a_{\mathrm{ef}}$ which increases with fixed reflection at absorbing and increasing reflection at non-absorbing wavelengths until the asymptotic limit is reached. Since this limit is decreasing with increasing absorbing wavelength, deviations of $a_{\mathrm{ef}}$ in ATSK3 are in general smaller than in SACURA. The consequences of the opposite situation where non-absorbing reflectance is fixed and absorbing reflectance decreases or increases can be seen in Fig. 22b and d. The degree of dependence between albedo at 1.6 μm and $\tau$ for optically thin clouds is similar to the case of 0.86-μm albedo since the albedo of the pixel used was around 0.11 so that the deviations of $\tau$ of about 2% to 5% correspond to similar absolute changes in ground albedo. This is not true for $a_{\mathrm{ef}}$ since absolute changes of albedo by $\pm 0.04$ lead to differences of the retrieved values
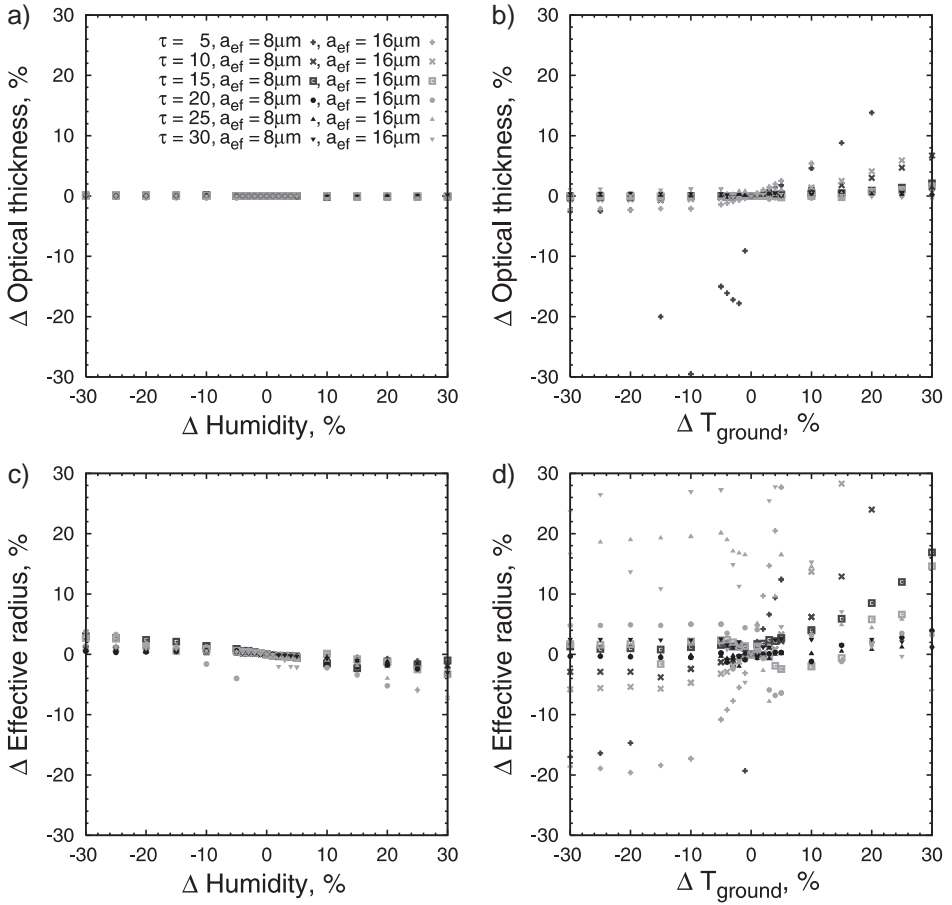
Fig. 21. Same as Fig. 20 but this time for uncertainties in auxiliary vertical humidity and ground temperature data.

exceeding 30% for small $\tau$ (note that this corresponds to an absolute change of the $a_{ef}$ values used that is still less than 3 μm). For $\tau > 10$ the differences are generally less than $\pm 10\%$. With increasing cloud thickness the influence on both $\tau$ and $a_{ef}$ decreases below $\pm 5\%$.

## 5. Conclusions

We have compared three different cloud retrievals algorithm and found very close results between them for a scene over ocean. The differences for a scene over land are much larger. We attribute this to the uncertainty related to the unknown surface albedo. This is treated in a different way in different algorithms. In particular, the results from SACURA are based on measurements at 0.86 μm, where the contribution from vegetation is particularly large.
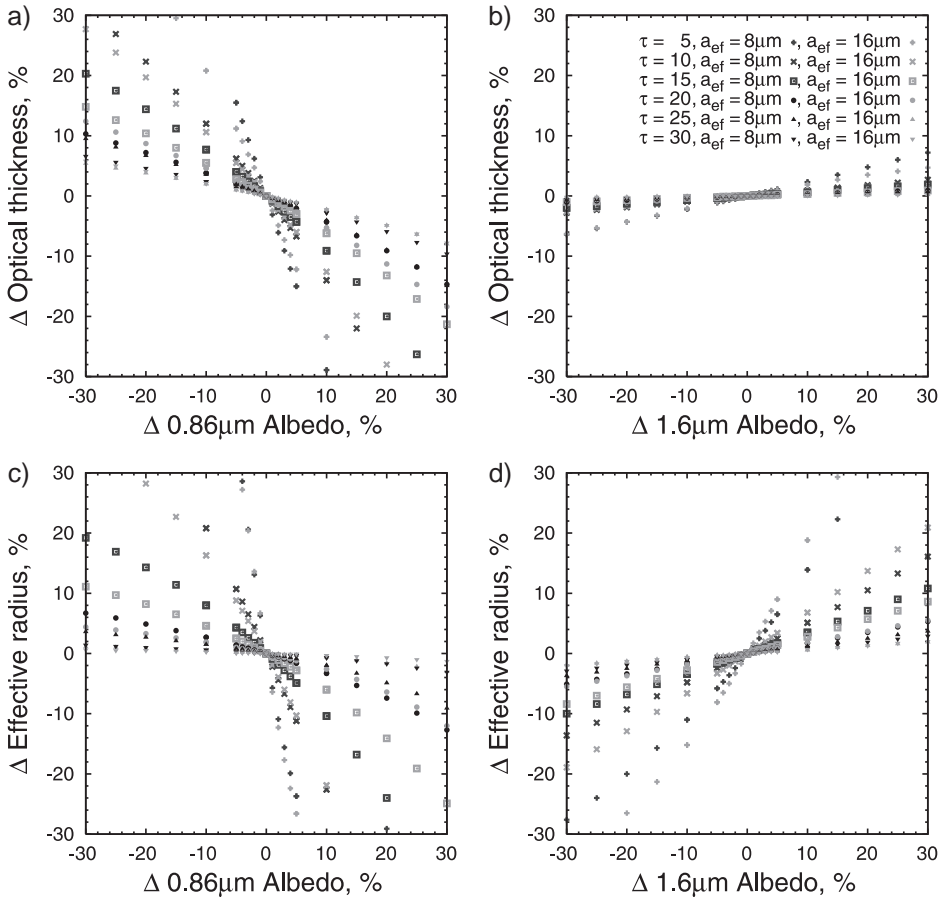
Fig. 22. Same as Fig. 20 but this time for the influence of errors in auxiliary ground albedo data for the non-absorbing (0.86 μm) and absorbing bands (1.6 μm) on the resulting optical thickness and effective cloud droplet radius of SACURA.

We underline that currently used cloud retrieval techniques provide values of cloud optical thickness that can differ by 10% on average (e.g., using MODIS and GLI cloud retrieval algorithms as applied to the same measurements but using different auxiliary information). The differences for the cloud effective radius are 15% on average. This should be taking into account while performing climatological studies, where cloud optical thickness, cloud effective radius, and cloud cover are main input parameters.

One important result of this work is to show that our simple retrieval technique provides results comparable with much more advanced codes. Therefore, SACURA can be used in these codes to generate a first guess or to reject unphysical results. It also can be used for physical insights in the cloud retrieval processes itself and data given in the paper can be used to check other existing cloud retrieval techniques as well. Moreover it can be used for other products like, e.g., rainfall retrievals where an accuracy of 10% is sufficient.

## Appendix A

*Symbols used in equations*

| | |
|---|---|
| $A_g$ | Lambertian ground albedo |
| $B$ | Planck function |
| $D$ | Geometrical cloud thickness |
| $F_0$ | Extraterrestrial solar flux |
| $K_0$ | Escape function for non-absorbing wavelengths |
| $K$ | Escape function for absorbing wavelengths |
| $L_c$ | Intensity of light reflected from a cloud |
| $L_{obs}$ | Observed radiance |
| $P(z)$ | Vertical air pressure profile |
| $P_g$ | Surface pressure |
| $R_\infty^0(\mu,\mu_0,\phi)$ | Reflection function of a non-absorbing, semi-infinite cloud |
| $R^0(\mu,\mu_0,\phi,\tau)$ | Reflection function of a non-absorbing finite cloud layer |
| $R_\infty(\mu,\mu_0,\phi)$ | Reflection function of an absorbing semi-infinite cloud |
| $R(\mu,\mu_0,\phi,\tau)$ | Reflection function of an absorbing finite cloud layer |
| $T(z)$ | Vertical air temperature profile |
| $T_c$ | Cloud-top temperature |
| $T_g$ | Ground temperature |
| $Z$ | Cloud-top height |
| $a_{ef}$ | Effective cloud droplet radius |
| $f$ | Atmospheric thermal emission |
| $g$ | Asymmetry parameter |
| $r_c$ | Unidirectional flux reflectivity of the cloud |
| $\bar{r}_c$ | Spherical albedo of a cloud |
| $t$ | Global transmittance of a cloud for absorbing wavelengths |
| $t_0$ | Diffuse transmittance of a cloud for non-absorbing wavelengths |
| $w(z)$ | Water vapour profile |
| $w_e$ | Equivalent water vapour amount above cloud |
| $\Theta$ | Unidirectional flux transmissivity |
| $\phi$ | Relative azimuth angle |
| $\mu$ | Cosine of satellite zenith angle |
| $\mu_0$ | Cosine of solar zenith angle |

| $\vartheta$ | Satellite zenith angle |
|---|---|
| $\vartheta_0$ | Solar zenith angle |
| $\tau$ | Optical thickness |
| $\omega$ | Single scattering albedo |

# References

Ackerman, S.A., Smith, W.L., Spinhirne, J.D., Revercomb, H.E., 1990. The 27–28 October 1986 FIRE IFO cirrus case study: spectral properties of cirrus clouds in the 8–12 μm window. Monthly Weather Review 118, 2377–2388.

Ackerman, S.A., Strabala, K.I., Menzel, W.P., Frey, R.A., Moeller, C.C., Gumley, L.E., 1998. Discriminating clear sky from clouds with MODIS. Journal of Geophysical Research 103, 32141–32157.

Arking, A., Childs, J.D., 1985. Retrieval of cloud cover parameters from multispectral satellite images. Journal of Applied Meteorology 24, 322–333.

Austin, P.H., Wang, Y., Pincus, R., Kujala, V., 1995. Precipitation in stratocumulus clouds 1995: observational and modelling results. Journal of the Atmospheric Sciences 52, 2329–2352.

Baum, B.A., Arduini, R.F., Wielicki, B.A., Minnis, P., Tsay, S.-C., 1994. Multilevel cloud retrieval using multispectral HIRS and AVHRR data: nighttime oceanic analysis. Journal of Geophysical Research 99, 5499–5514.

Baum, B.A., Frey, R.A., Mace, G.G., Harkey, M.K., Yang, P., 2003. Nighttime multilayered cloud detection using MODIS and ARM data. Journal of Applied Meteorology 42, 905–919.

Berk, A., Bernstein, L.S., Anderson, G.P., Acharya, P.K., Robertson, D.C., Chetwynd, J.H., Adler-Golden, S.M., 1998. MODTRAN cloud and multiple scattering upgrades with application to AVIRIS. Remote Sensing of Environment 65, 367–375.

Bovensmann, H., Burrows, J.P., Buchwitz, M., Frerick, J., Nõel, S., Rozanov, V.V., Chance, K.V., Goede, A.P.H., 1999. SCIAMACHY: mission objectives and measurement modes. Journal of the Atmospheric Sciences 56, 127–149.

Bretherton, C.S., Uttal, T., Fairall, C.W., Yuter, S.E., Weller, R.A., Baumgardner, D., Comstock, K., Wood, R., Raga, G.B., 2004. The EPIC 2001 stratocumulus study. Bulletin of the American Meteorological Society 85, 967–977.

Germogenova, T.A., 1963. Some formulas to solve the transfer equation in the plane layer problem. In: Stepanov, B.I. (Ed.), Spectroscopy of Scattering Media. BSSR, Minsk, pp. 36–41.

Han, Q., Rossow, W.B., Lacis, A.A., 1994. Near-global survey of effective droplet radii in liquid water clouds using ISCCP data. Journal of Climate 7, 465–497.

Han, Q., Rossow, W., Welch, R., White, A., Chou, J., 1995. Validation of satellite retrievals of cloud microphysics and liquid water path using observations from FIRE. Journal of the Atmospheric Sciences 52, 4183–4195.

Kawamoto, K., Nakajima, T., Nakajima, T.Y., 2001. A global determination of cloud microphysics with AVHRR remote sensing. Journal of Climate 14, 2054–2068.

Kiehl, J.T., 1994. Sensitivity of a GCM climate simulation to differences in continental versus maritime cloud drop size. Journal of Geophysical Research 99, 23107–23115.

King, M.D., 1987. Determination of the scaled optical thickness of clouds from reflected solar radiation measurements. Journal of the Atmospheric Sciences 44, 1734–1751.

King, M.D., Greenstone, R. (Eds.), 1999a. EOS Reference Handbook. NASA Goddard Space Flight Center, Greenbelt, MD (Rep. NASA NP-1999-08-134-GSFC, 361 pp.).

King, M. D., Greenstone, R., 1999b. EOS Reference Handbook. Goddard Space Flight Center. Available online at http://eospso.gsfc.nasa.gov/ftp_docs/handbook99.pdf.

King, M.D., Kaufman, Y.J., Menzel, W.P., Tanré, D., 1992. Remote sensing of cloud, aerosol, and water vapor properties from the moderate resolution imaging spectrometer (MODIS). IEEE Transactions on Geoscience and Remote Sensing 30, 2–27.

King, M.D., Tsay, S.-C., Platnick, S.E., Wang, M., Liou, K.-N., 1997. Cloud Retrieval Algorithms for MODIS: Optical Thickness, Effective Particle Radius, and Thermodynamic Phase. NASA.

Kokhanovsky, A.A., 2004a. Optical properties of terrestrial clouds. Earth-Science Reviews 64, 189–241.

Kokhanovsky, A.A., 2004b. Light Scattering Media Optics, 3rd edition. Springer Verlag, Berlin.

Kokhanovsky, A.A., 2004c. Reflection of light from nonabsorbing semi-infinite cloudy media: a simple approximation. Journal of Quantitative Spectroscopy & Radiative Transfer 85, 25–33.

Kokhanovsky, A.A., 2004d. The depth of sunlight penetration in the cloud fields for remote sensing. IEEE Geoscience and Remote Sensing Letters 1, 242–245.

Kokhanovsky, A.A., Rozanov, V.V., 2003. The reflection function of optically thick weakly absorbing turbid layers: a simple approximation. Journal of Quantitative Spectroscopy & Radiative Transfer 77, 165–175.

Kokhanovsky, A.A., Rozanov, V.V., Zege, P.E., Bovensmann, H., Burrows, J.P., 2003. A semianalytical cloud retrieval algorithm using backscattered radiation in 0.4–2.4 μm spectral region. Journal of Geophysical Research 108, 4-1–4-19.

Kokhanovsky, A.A., Rozanov, V.V., Vountas, M., Buchwitz, M., Burrows, J.P., 2004. Semi-analytical cloud retrieval algorithm for SCIAMACHY/ENVISAT. Algorithm Theoretical Basis Document.

Kokhanovsky, A.A., Rozanov, V.V., Nauss, T., Reudenbach, C., Daniel, J.S., Miller, H.L., Burrows, J.P., 2005. The semianalytical cloud retrieval algorithm for SCIAMACHY. I: the validation. Atmospheric Chemistry and Physics, 1995–2015 (Discussion 5).

Liou, K.-N., Wittman, G.D., 1979. Parameterization of the radiative properties of clouds. Journal of the Atmospheric Sciences 36, 1261–1273.

Loeb, N.G., Davies, R., 1996. Observational evidence of plane parallel model biases: the apparent dependence of cloud optical depth on solar zenith angle. Journal of Geophysical Research 101, 1621–1634.

Lucht, W., Schaaf, C.B., Strahler, A.H., 2000. An algorithm for the retrieval of albedo from space using semiempirical BRDF models. IEEE Transactions on Geoscience and Remote Sensing 38, 977–998.

Min, Q., Minnis, P., Khaiyer, M.M., 2004. Comparison of cirrus optical thickness depths derived from GOES 8 and surface measurements. Journal of Geophysical Research 109, D15207.

Mishchenko, M.I., Dlugach, J.M., Yanovitskij, E.G., Zakharova, N.T., 1999. Bidirectional reflectance of flat, optically thick particulate layers: an efficient radiative transfer solution and applications to snow and soil surfaces. Journal of Quantitative Spectroscopy & Radiative Transfer 63, 409–432.

Nakajima, T., King, M.D., 1990. Determination of the optical thickness and effective particle radius of clouds from reflected solar radiation measurements: Part I. Theory. Journal of the Atmospheric Sciences 47, 1878–1893.

Nakajima, T., King, M.D., 1992. Asymptotic theory for optically thick layers: Application to the discrete ordinates method. Applied Optics 31, 7669–7683.

Nakajima, T.Y., Nakajima, T., 1995. Wide-area determination of cloud microphysical properties from NOAA AVHRR measurements for FIRE and ASTEX regions. Journal of the Atmospheric Sciences 52, 4043–4059.

Nakajima, T., Tanaka, M., 1986. Matrix formulations for the transfer of solar radiation in a plane-parallel scattering atmosphere. Journal of Quantitative Spectroscopy & Radiative Transfer 35, 13–21.

Nakajima, T., Tanaka, M., 1988. Algorithms for radiative intensities calculations in moderately thick areas using a truncation approximation. Journal of Quantitative Spectroscopy & Radiative Transfer 40, 51–69.

Nakajima, T., King, D.M., Spinhirne, L.F., Radke, J.D., 1991. Determination of the optical thickness and effective particle radius of clouds from reflected solar radiation measurements: Part II. Marine stratocumulus observations. Journal of the Atmospheric Sciences 48, 728–750.

Nakajima, T.Y., Nakajima, T., Nakajima, M., Fukushima, H., Kuji, M., Uchiyama, A., Kishino, M., 1998. Optimization of the advanced earth observing satellite II global imager channels by use of radiative transfer calculations. Applied Optics 15, 3149–3163.

Nauss, T., Bendix, J., in press. An operational MODIS processing scheme for PC dedicated to direct broadcasting applications in meteorology and earth sciences. Computers & Geosciences.

Nikolaeva, O.V., Bass, L.P., Germogenova, T.A., Kokhanovsky, A.A., Kuznetsov, V.S., Mayer, B., 2005. The influence of neighbouring clouds on the clear sky reflectance studied using the 3-D transport code RADUGA. Journal of Quantitative Spectroscopy and Radiative Transfer 94, 405–424.

Pérez, J.C., Herrera, F., Rosa, F., González, A., Wetzel, M.A., Borys, R.D., Lowenthal, D.H., 2000. Retrieval of marine stratus cloud droplet size from NOAA-AVHRR night-time imagery. Remote Sensing of Environment 73, 31–45.

Platnick, S., 2000. Vertical photon transport in cloud remote sensing problems. Journal of Geophysical Research 105, 22919–22935.

Platnick, S., Valero, F.P.J., 1995. A validation of a satellite cloud retrieval during ASTEX. Journal of the Atmospheric Sciences 52, 2985–3001.

Platnick, S., King, M.D., Ackerman, S.A., Menzel, W.P., Baum, B.A., Rièdi, J.C., Frey, R.A., 2003. The MODIS cloud products: algorithms and examples from Terra. IEEE Transactions on Geoscience and Remote Sensing 41, 459–473.

Rosenfeld, D., Cattani, E., Melanie, S., Levizzani, V., 2004. Conseiderations on dalyight operation of 1.6-versus 3.7μm channel on NOAA and METOP satellites. Bulletin of the American Meteorological Society 85, 873–881.

Strabala, K.I., Ackerman, S.A., Menzel, W.P., 1994. Cloud properties inferred from 8–12 μm data. Journal of Applied Meteorology 33, 212–229.

Twomey, S., 1991. Aerosols, clouds and radiation. Atmospheric Environment 25a, 2435–2442.

van de Hulst, H.C., 1980. Multiple Light Scattering: Tables, Formulas and Applications. Academic Press, New York.

Várnai, T., 2000. Influence of three-dimensional radiative effects on the spatial distribution of shortwave cloud reflection. Journal of the Atmospheric Sciences 57, 216–229.

Vermote, E., Roger, J.C., 1996. Radiative transfer modeling for calibration and atmospheric correction. In: d'Souza, G., Belward, A.S., Malingreau, J.-P. (Eds.), Advances in the Use of NOAA AVHRR Data for Land Applications, vol. 5. Springer, Berlin, pp. 49–72.

Vermote, E.F., Tanré, D., Deuzé, J.L., Herman, M., Morcrette, J.-J., 1997a. Second simulation of the satellite signal in the solar spectrum, 6s: an overview. IEEE Transactions on Geoscience and Remote Sensing 35, 675–686.

Vermote, E., Tanré, D., Deuzé, J.L., Herman, M., Morcrette, J.-J., 1997b. Second Simulation of the Satellite Signal in the Solar Spectrum (6S). 6S User Guide Version 2.

Zege, E.P., Ivanov, A.P., Katsev, I.L., 1991. Image Transfer Through a Scattering Medium. Springer, New York.